JOURNAL OF COMPUTATIONAL PHYSICS 60, 391–436 (1985)

Finite Difference Simulation of Nonlinear Waves Generated by Ships of Arbitrary Three-Dimensional Configuration

HIDEAKI MIYATA AND SHINICHI NISHIMURA

Department of Naval Architecture, University of Tokyo, Tokyo, Japan

AND

AKIRA MASUKO

Research Institute, Ishikawajima-Harima Heavy Industries, Tokyo, Japan

Received April 17, 1984; revised September 12, 1984

A modified marker-and-cell method is developed in order to simulate nonlinear wave making in the near-field of ships of arbitrary three-dimensional (3D) configuration advancing steadily in deep water. The 3D Navier–Stokes equations are solved by a finite difference scheme under proper boundary conditions. Efforts are particularly focused on the treatment of the boundary conditions on the body surface and free surface which have complicated 3D configurations. An orthogonal cell system with more than 70,000 cells is used for the computation of the waves and flow field of ships. The agreement of computational results with experiment is good, and it promises effectiveness for engineering purposes.

I. INTRODUCTION

Water waves have a dispersive or dissipative property. Concerning classical gravitational waves on the water surface, dispersion is very important if the water is deep enough. The waves of a ship on a steady straight course were considered as a typical example of a linear dispersive wave, which is called Kelvin's wave system. This is why linear potential theories with linearized free surface condition were applied to the ship wave problem. However, the linear theories still do not succeed

0021-9991/85 $3.00

in explaining the ship wave system or estimating the ship wave resistance. The discrepancy is not only quantitative but also qualitative sometimes.

Recently it was experimentally clarified that the inadequacy of linear wave-making theories is due to the nonlinear features of waves generated by ships. Ships advancing steadily in deep water generate steep nonlinear waves called free surface shock waves (FSSW) in the near field of ships; consequently, the breaking of waves and energy-deficient phenomena take place on the wave front (see [1–3]). Therefore, the energy of nonlinear waves in the near field of ships is partly dissipated into momentum loss far behind, partly spread to the far field by dispersion. The latter constitutes Kelvin's wave system. Ship waves have both dissipative and dispersive properties.

A number of wave-making resistance theories have been developed, but they all are based on various linearizations of the problem. A very few of them fulfills the exact nonlinear free surface condition. Since the characteristics of the nonlinear ship waves indicate the importance of the nonlinear free surface condition, a new nonlinear theoretical solution method needs to be developed. The most powerful and flexible method is supposed to be a finite difference method which is suitable for nonlinear problems with free surface. One of the most famous methods is the MAC method by Welch *et al.* [4], and some improved versions have been developed by, for example, Chan and Street [5], Viecelli [6], and Nichols and Hirt [7]. This kind of method is a solution procedure for Navier–Stokes equations and the equation of continuity. When exact boundary conditions are properly treated, the generation of nonlinear steep waves can be explained by this kind of procedure, although subsequent energy-deficient phenomena of wave breaking and free surface turbulence cannot be taken into consideration.

The authors and colleagues have developed a modified version of the MAC method called the TUMMAC method (Tokyo University modified marker-and-cell method) by particularly modifying the body boundary condition and the free surface condition to suit to the ship wave problem. These two boundaries occur where nonlinear fluid phenomena are initiated. The versions TUMMAC-I (see [8–10]) and TUMMAC-II (see [11, 12]) were already developed for waves from a wedge model and from the fore-part of a hull with arbitrary horizontal configuration but with vertical walls, respectively.

In this report a new version called TUMMAC-IV for arbitrary 3-dimensional (3D) hull configuration is developed. The degree of accuracy is raised by the use of a modified finite differencing of convective terms and by careful treatment of every boundary conditions. In particular, a new treatment of body boundary conditions for arbitrary 3D configurations is proposed in the framework of a rectangular cell system. Since for the flow field that contains both a free surface that is deformed and a body surface of complicated configurations that pierces it, the application of a body-fitted coordinate system gives rise to some serious difficulties; the TUMMAC-IV method will be very useful for practical engineering purposes.

In Sections II and III governing equations, finite difference representations and the computational procedure are described. In Section IV the solution of the

Poission equation is described, and the stability condition is examined in Section V. The explanations of various boundary conditions are present in Sections VI to X. Computed results are presented and discussed in Section XI for simple ships with vertical walls and in Section XII for hull forms of completely arbitrary configuration. Brief conclusions are mentioned in Section XIII.

II. Governing Equations

The governing equations for incompressible fluid flow are the equation of continuity and the Navier–Stokes (NS) equations as follow:

$$\partial u/\partial x + \partial v/\partial y + \partial w/\partial z = 0 \tag{1}$$

$$\begin{aligned}
&\partial u/\partial t + \partial(u^2)/\partial x + \partial(uv)/\partial y + \partial(uw)/\partial z \\
&\quad = -\partial \Psi/\partial x + \nu(\partial^2 u/\partial x^2 + \partial^2 u/\partial y^2 + \partial^2 u/\partial z^2) \\
&\partial v/\partial t + \partial(uv)/\partial x + \partial(v^2)/\partial y + \partial(vw)/\partial z \\
&\quad = -\partial \Psi/\partial y + \nu(\partial^2 v/\partial x^2 + \partial^2 v/\partial y^2 + \partial^2 v/\partial z^2) \\
&\partial w/\partial t + \partial(uw)/\partial x + \partial(vw)/\partial y + \partial(w^2)/\partial z \\
&\quad = -\partial \Psi/\partial z + \nu(\partial^2 w/\partial x^2 + \partial^2 w/\partial y^2 + \partial^2 w/\partial z^2) + g.
\end{aligned} \tag{2}$$

Here the Cartesian coordinate system (x, y, z) is employed and velocity components are u, v, and w in respective direction. Ψ is pressure divided by the density, ν the kinematic viscosity, and g the gravitational acceleration. The employment of the most fundamental equations is of first importance for the simulation of nonlinear phenomena.

Of secondary importance is the treatment of boundary conditions on the free surface and body surface. On the free surface both dynamical and kinematic conditions must be satisfied. The former is that the pressure on the free surface accords with the atmospheric pressure, and the latter is that water particles move along the free surface and do not go across it, if viscous stress on the free surface is ignored. The body boundary condition is the same with the above kinematic condition which means that the velocity normal to the body boundary is zero on the boundary.

It is generally supposed that the waves generated by the fore half-body are scarcely influenced by the boundary layer covers the ship surface but that those generated by the after half-body interact with the viscous flow in the vicinity of a ship. Therefore, it is desirable to apply the viscous body boundary condition for the complete simulation of ship waves. However, in this 3D problem the cell size cannot be so small as to resolve the viscous fluid motion. Thus, in computations in this paper, viscous effects on both free surface and body surface are not taken into consideration. The main aim of this paper is to simulate ship waves, which are scarcely influenced by viscous effects, under exact inviscid boundary conditions. In par-

ticular, the free surface condition is nonlinear and it is imposed on the exact location of free surface that is not known beforehand but determined through the course of computation.

III. Finite Difference Representation and Computational Procedure

The origin of the Cartesian coordinate system (x, y, z) is at the forward end of a ship on the undisturbed free surface. The x axis is taken to be along the ship centerline being positive aftward, the y axis is laterally oriented, and the z axis vertically is positive upward.

A staggered mesh system is used as shown in Fig. 1. Pressure is defined at the center of the cell volume and velocities on the center of the cell surfaces. The subscripts i, j, and k are used for the cell location. The center of the cell volume is at (i, j, k).

By forward differencing in time and centered differencing in space, Eqs. (2) become:

$$
\begin{aligned}
&(u^{n+1}_{i+1/2,j,k} - u_{i+1/2,j,k})/\mathrm{DT} \\
&\quad = -U_{Ci+1/2,j,k} - (\Psi_{i+1,j,k} - \Psi_{i,j,k})/\mathrm{DX} \\
&\qquad + \nu[(u_{i+3/2,j,k} - 2u_{i+1/2,j,k} + u_{i-1/2,j,k})/\mathrm{DX}^2 \\
&\qquad + (u_{i+1/2,j+1,k} - 2u_{i+1/2,j,k} + u_{i+1/2,j-1,k})/\mathrm{DY}^2 \\
&\qquad + (u_{i+1/2,j,k+1} - 2u_{i+1/2,j,k} + u_{i+1/2,j,k-1})/\mathrm{DZ}^2], \\
&(v^{n+1}_{i,j+1/2,k} - v_{i,j+1/2,k})/\mathrm{DT} \\
&\quad = -V_{Ci,j+1/2,k} - (\Psi_{i,j+1,k} - \Psi_{i,j,k})/\mathrm{DY} \\
&\qquad + \cdots, \\
&(w^{n+1}_{i,j,k+1/2} - w_{i,j,k+1/2})/\mathrm{DT} \\
&\quad = -W_{Ci,j,k+1/2} - (\Psi_{i,j,k+1} - \Psi_{i,j,k})/\mathrm{DZ} \\
&\qquad + \mathrm{g} + \cdots.
\end{aligned}
\tag{3}
$$

Here DT is time increment DX, DY, DZ are distances between velocity points in x, y, z directions, respectively, i.e., length, width and height of a cell. Superscripts are used for the time level i.e., variables with superscript $(n+1)$ are related to the $(n+1)$th time step and variables lacking a superscript are evaluated at the nth step. It is noted that since the time-differencing in Eqs. (3) is an approximation for the time level $n+\frac{1}{2}$, the remaining terms can be evaluated at either time level n or $n+1$. Here, they are evaluated at the time level n. The convection terms are denoted U_C, V_C, and W_C of which expression is described afterward.

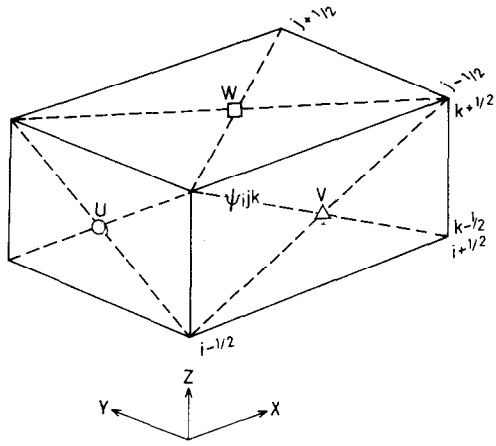

FIG. 1. Definition sketch of staggered mesh system.

The expression for the velocity components at the $(n+1)$th time step is derived from Eqs. (3) by combining the terms except the pressure gradient term and denoting them ξ, η, and ζ as:

$$\begin{aligned} u^{n+1}_{i+1/2,j,k} &= \xi_{i+1/2,j,k} - (\Psi_{i+1,j,k} - \Psi_{i,j,k})\,\mathrm{DT/DX} \\ v^{n+1}_{i,j+1/2,k} &= \eta_{i,j+1/2,k} - (\Psi_{i,j+1,k} - \Psi_{i,j,k})\,\mathrm{DT/DY} \\ w^{n+1}_{i,j,k+1/2} &= \zeta_{i,j,k+1/2} - (\Psi_{i,j,k+1} - \Psi_{i,j,k})\,\mathrm{DT/DZ} \end{aligned} \tag{4}$$

where

$$\begin{aligned} \xi_{i+1/2,j,k} &= u_{i+1/2,j,k} - \mathrm{DT}\cdot U_{Ci+1/2,j,k} \\ &\quad + \nu\cdot\mathrm{DT}\,[(u_{i+3/2,j,k} - 2u_{i+1/2,j,k} + u_{i-1/2,j,k})/\mathrm{DX}^2 \\ &\quad + (u_{i+1/2,j+1,k} - 2u_{i+1/2,j,k} + u_{i+1/2,j-1,k})/\mathrm{DY}^2 \\ &\quad + (u_{i+1/2,j,k+1} - 2u_{i+1/2,j,k} + u_{i+1/2,j,k-1})/\mathrm{DZ}^2] \\ \eta_{i,j+1/2,k} &= v_{i,j+1/2,k} - \mathrm{DT}\cdot \mathrm{V}_{Ci,j+1/2,k} + \nu\cdot\mathrm{DT}\,[\cdots] \\ \zeta_{i,j,k+1/2} &= w_{i,j,k+1/2} - \mathrm{DT}\cdot \mathrm{W}_{Ci,j,k+1/2} + \nu\cdot\mathrm{DT}\,[\cdots] + g. \end{aligned} \tag{5}$$

For the finite difference representation of the convective terms denoted U_C, V_C, and W_C the combination of the second-order upstream differencing (donor-cell method) and the centered differencing is employed following Hirt *et al.*, [13]. The x-directional convective term U_C at $i+\frac{1}{2}$ is expressed as

$$\begin{aligned} U_{Ci+1/2,j,k} &= (1/\mathrm{DX})\,[(u^2)_{i+1,j,k} - (u^2)_{i,j,k}] \\ &\quad + (1/\mathrm{DY})[(uv)_{i+1/2,j+1/2,k} - (uv)_{i+1/2,j-1/2,k}] \\ &\quad + (1/\mathrm{DZ})\,[(uw)_{i+1/2,j,k+1/2} - (uw)_{i+1/2,j,k-1/2}] \end{aligned} \tag{6}$$

where the first term is, for example,

$$
\begin{aligned}
&(1/\mathrm{DX})\,[(u^2)_{i+1,j,k}-(u^2)_{i,j,k}]\\
&\quad=\{1/(4\cdot\mathrm{DX})\}\,[\{(u_{i+1/2,j,k}+u_{i+3/2,j,k})^2-(u_{i-1/2,j,k}+u_{i+1/2,j,k})^2\}\\
&\qquad+\alpha\{|u_{i+1/2,j,k}+u_{i+3/2,j,k}|\cdot(u_{i+1/2,j,k}-u_{i+3/2,j,k})\\
&\qquad-|u_{i-1/2,j,k}+u_{i+1/2,j,k}|\cdot(u_{i-1/2,j,k}-u_{i+1/2,j,k})\}\,].
\end{aligned}
\tag{7}
$$

Velocity points are shown in Fig. 2. When $\alpha=0$, it is centered differencing, and when $\alpha=1$, the donor-cell method. The value of α is so determined as to satisfy the stability condition described in a following section and to minimize the numerical dissipation to which the finite difference error of the donor-cell differencing mostly contributes.

The divergence D at the $(n+1)$th time step is obtained from Eqs. (1) and (4).

$$
\begin{aligned}
D^{n+1}_{i,j,k}&=(u^{n+1}_{i+1/2,j,k}-u^{n+1}_{i-1/2,j,k})/\mathrm{DX}+(v^{n+1}_{i,j+1/2,k}-v^{n+1}_{i,j-1/2,k})/\mathrm{DY}\\
&\quad+(w^{n+1}_{i,j,k+1/2}-w^{n+1}_{i,j,k-1/2})/\mathrm{DZ}\\
&=(\xi_{i+1/2,j,k}-\xi_{i-1/2,j,k})/\mathrm{DX}+(\eta_{i,j+1/2,k}-\eta_{i,j-1/2,k})/\mathrm{DY}\\
&\quad+(\zeta_{i,j,k+1/2}-\zeta_{i,j,k-1/2})/\mathrm{DZ}\\
&\quad+(\mathrm{DT}/\mathrm{DX}^2)\,(2\Psi_{i,j,k}-\Psi_{i+1,j,k}-\Psi_{i-1,j,k})\\
&\quad+(\mathrm{DT}/\mathrm{DY}^2)\,(2\Psi_{i,j,k}-\Psi_{i,j+1,k}-\Psi_{i,j-1,k})\\
&\quad+(\mathrm{DT}/\mathrm{DZ}^2)\,(2\Psi_{i,j,k}-\Psi_{i,j,k+1}-\Psi_{i,j,k-1}).
\end{aligned}
\tag{8}
$$

$D=0$ is required to rigorously conserve mass and it is aimed at the $(n+1)$th time step, i.e., $D^{n+1}_{i,j,k}$ in Eq. (8) is set at zero. Then, the equation for the pressure is derived as

$$
\begin{aligned}
\Psi_{i,j,k}&=(1/\mathrm{AA})\,[(\Psi_{i+1,j,k}+\Psi_{i-1,j,k})/\mathrm{DX}^2+(\Psi_{i,j+1,k}+\Psi_{i,j-1,k})/\mathrm{DY}^2\\
&\quad+(\Psi_{i,j,k+1}+\Psi_{i,j,k-1})/\mathrm{DZ}^2-R_{i,j,k}]
\end{aligned}
\tag{9}
$$

where

$$
\mathrm{AA}=2(1/\mathrm{DX}^2+1/\mathrm{DY}^2+1/\mathrm{DZ}^2) \tag{10}
$$

$$
\begin{aligned}
R_{i,j,k}&=(\xi_{i+1/2,j,k}-\xi_{i-1/2,j,k})/(\mathrm{DT}\cdot\mathrm{DX})\\
&\quad+(\eta_{i,j+1/2,k}-\eta_{i,j-1/2,k})/(\mathrm{DT}\cdot\mathrm{DY})\\
&\quad+(\zeta_{i,j,k+1/2}-\zeta_{i,j,k-1/2})/(\mathrm{DT}\cdot\mathrm{DZ}).
\end{aligned}
\tag{11}
$$

$R_{i,j,k}$ is a source term of the Poisson equation (9) and is determined from the velocity field through (5).

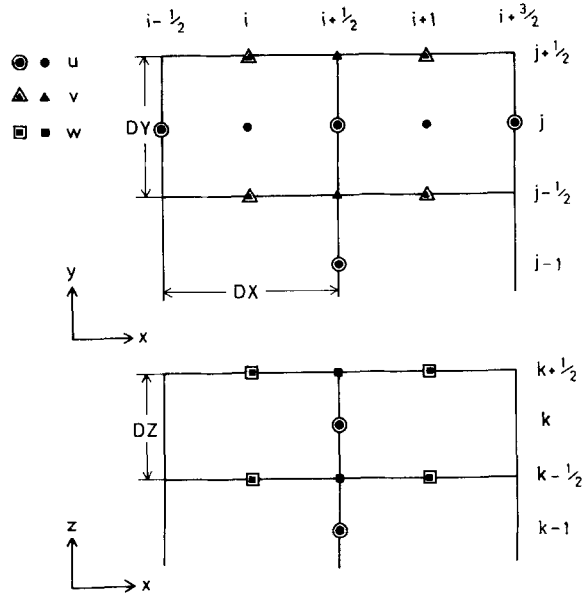

FIG. 2. Velocity points for the second-order upstream differencing (u-component).

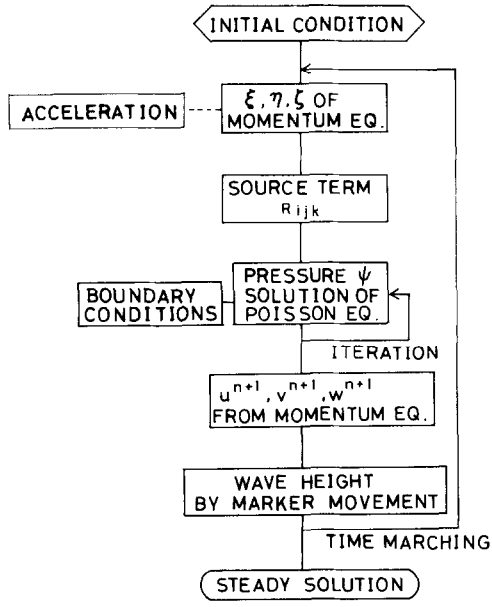

FIG. 3. Block diagram of the TUMMAC-IV scheme.

The momentum equations (4) and the Poisson equation (9) are the principal equations to be solved. Equations (4) are hyperbolic equations to be solved as an initial-value problem and Eq. (9) is an elliptic equation to be solved as a boundary-value problem. Equations (4) are solved by time-marching and at every time step Eq. (9) is solved by an iterative procedure.

The solution is advanced in time by a series of repeated steps. First the Poisson equation (9) is iteratively solved under given initial and boundary conditions, and then new velocity components are derived from the momentum equations (4). A new source term $R_{i,j,k}$ for the Poisson equation (9) is calculated by the new velocity field. Marker particles are used to tell the new location of free surface. And then the cycle is repeated. A block diagram is presented in Fig. 3.

This solution algorithm is suitable to unsteady problems, although it is applied to a steady wave-making problem in this work by letting an unsteady solution approach a steady state. The computation is started from rest condition, and velocities at the inflow and bottom boundaries are gradually accelerated for several hundred time steps. After the steps of acceleration the computation is continued for adequate time steps until a steady state is reached with the velocities at the two boundaries kept unchanged.

IV. Solution of the Poisson Equation

The Poisson equation (9) is iteratively solved by the following equation:

$$\Psi^{m+1}_{i,j,k} = \Psi^{m}_{i,j,k} + \omega(\Psi^{m+1}_{i,j,k\,\mathrm{cal}} - \Psi^{m}_{i,j,k}) \tag{12}$$

The superscripts m and $(m+1)$ denote iteration number and ω is a relaxation factor. The iteration is continued until the difference of pressure between the two iterative steps, i.e., the second term of Eq. (12) converges within an allowable error.

The successive over-relaxation (SOR) method is employed, and $\Psi^{m+1}_{i,j,k\,\mathrm{cal}}$ in

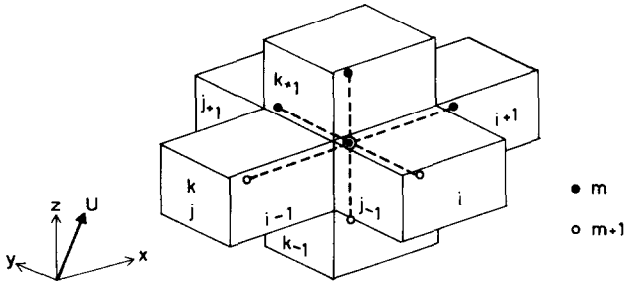

FIG. 4. Pressure points for SOR method.

Eq. (12) is calculated from Eq. (9) as below in Eq. 13, while the pressure points are shown in Fig. 4:

$$\begin{aligned}\Psi^{m+1}_{i,j,k\,\mathrm{cal}} = (1/\mathrm{AA})[&(\Psi^{m}_{i+1,j,k} + \Psi^{m+1}_{i-1,j,k})/\mathrm{DX}^2 \\ &+ (\Psi^{m}_{i,j+1,k} + \Psi^{m+1}_{i,j-1,k})/\mathrm{DY}^2 \\ &+ (\Psi^{m}_{i,j,k+1} + \Psi^{m+1}_{i,j,k-1})/\mathrm{DZ}^2 - R_{i,j,k}].\end{aligned} \tag{13}$$

By substituting Eq. (13) into Eq. (12), we obtain the following equation to be solved by the SOR method:

$$\begin{aligned}\Psi^{m+1}_{i,j,k} = (1-\omega)\Psi^{m}_{i,j,k} + (\omega/\mathrm{AA})[&(\Psi^{m}_{i+1,j,k} + \Psi^{m+1}_{i-1,j,k})/\mathrm{DX}^2 \\ &+ (\Psi^{m}_{i,j+1,k} + \Psi^{m+1}_{i,j-1,k})/\mathrm{DY}^2 \\ &+ (\Psi^{m}_{i,j,k+1} + \Psi^{m}_{i,j,k-1})/\mathrm{DZ}^2 - R_{i,j,k}].\end{aligned} \tag{14}$$

The term in the parentheses in Eq. (12) is modified by eliminating $\Psi^{m+1}_{i,j,k\,\mathrm{cal}}$ and ξ, η, ζ in $R_{i,j,k}$ making use of Eqs. (4), (10), (11), and (13) as follows:

$$\begin{aligned}\Psi^{m+1}_{i,j,k\,\mathrm{cal}} - \Psi^{m}_{i,j,k} = (1/\mathrm{AA})[&\{(\Psi^{m}_{i+1,j,k} - \Psi^{m}_{i,j,k})/\mathrm{DX}^2 - \xi_{i+1/2,j,k}/(\mathrm{DT}\cdot\mathrm{DX})\} \\ &- \{(\Psi^{m}_{i,j,k} - \Psi^{m+1}_{i-1,j,k})/\mathrm{DX}^2 - \xi_{i-1/2,j,k}/(\mathrm{DT}\cdot\mathrm{DX})\} \\ &+ \{(\Psi^{m}_{i,j+1,k} - \Psi^{m}_{i,j,k})/\mathrm{DY}^2 - \eta_{i,j+1/2,k}/(\mathrm{DT}\cdot\mathrm{DY})\} \\ &- \{(\Psi^{m}_{i,j,k} - \Psi^{m+1}_{i,j-1,k})/\mathrm{DY}^2 - \eta_{i,j-1/2,k}/(\mathrm{DT}\cdot\mathrm{DY})\} \\ &+ \{(\Psi^{m}_{i,j,k+1} - \Psi^{m}_{i,j,k})\mathrm{DZ}^2 - \zeta_{i,j,k+1/2}/(\mathrm{DT}\cdot\mathrm{DZ})\} \\ &- \{(\Psi^{m}_{i,j,k} - \Psi^{m+1}_{i,j,k-1})/\mathrm{DZ}^2 - \zeta_{i,j,k-1/2}/(\mathrm{DT}\cdot\mathrm{DZ})\}\end{aligned} \tag{15}$$

$$\begin{aligned}= \{1/(\mathrm{DT}\cdot\mathrm{AA})\}\{&(u^{m+1/2}_{i-1/2,j,k} - u^{m}_{i+1/2,j,k})/\mathrm{DX} \\ &+ (v^{m+1/2}_{i,j-1/2,k} - v^{m}_{i,j+1/2,k})/\mathrm{DY} \\ &+ (w^{m+1/2}_{i,j,k-1/2} - w^{m}_{i,j,k+1/2})/\mathrm{DZ}\} \\ \approx -\{&1/(\mathrm{DT}\cdot\mathrm{AA})\}\,[D^{m}_{i,j,k}].\end{aligned}$$

In the above derivation the superscript $(m+\frac{1}{2})$ is used for the velocities calculated by pressure at two iterative steps m and $(m+1)$. The divergence $D^m_{i,j,k}$ is assumed as defined above. Then, Eq. (12) is rewritten as

$$\Psi^{m+1}_{i,j,k} = \Psi^m_{i,j,k} - \{\omega/(\mathrm{DT}\cdot \mathrm{AA})\}[D^m_{i,j,k}]. \tag{16}$$

The solution method by Eq. (16) is the simultaneous iterative method which is a modification of and equivalent to the SOR method. In this method velocities are successively updated through Eqs. (4) so that D in Eq. (16) is calculated immediately after the neighboring pressure is computed at every iterative step, whereas the terms ξ, η, and ζ are kept unchanged throughout the iteration. Therefore in this velocity–pressure iteration, pressure is evaluated at the time level $n+1$ and the remaining terms of the momentum equations are evaluated at the level n. This procedure is convenient to deal with the boundary condition for an arbitrary body configuration.

V. The Numerical Stability Condition

In order to obtain stable solutions some conditions must be satisfied in the computation of the NS-equations and the Poisson equation. Neumann's method [14] or Hirt's method [15] of stability analysis is often applied. These methods are valid for linear equations, and therefore, the finite-difference equations are linearized by assumptions. Moreover, a pressure gradient term and a gravitational term are ignored. Thus, these analyses give only approximate conditions.

The stability consideration based on the Neumann's method gives the following conditions when the donor-cell method is employed for the differencing of the convective terms [10]:

$$(c_x + c_y + c_z)^2 \leqslant (c_x + c_y + c_z) + 2(d_x + d_y + d_z) \leqslant 1. \tag{17}$$

Here c_x, c_y, c_z are Courant numbers and d_x, d_y, d_z diffusion numbers defined as:

$$c_x = u\cdot\frac{\mathrm{DT}}{\mathrm{DX}}, \qquad c_y = v\cdot\frac{\mathrm{DT}}{\mathrm{DY}}, \qquad c_z = w\cdot\frac{\mathrm{DT}}{\mathrm{DZ}} \tag{18}$$

$$d_x = \nu\cdot\frac{\mathrm{DT}}{\mathrm{DX}^2}, \qquad d_y = \nu\cdot\frac{\mathrm{DT}}{\mathrm{DY}^2}, \qquad d_z = \nu\cdot\frac{\mathrm{DT}}{\mathrm{DZ}^2}. \tag{19}$$

Equation (17) is decomposed into the following two conditions:

$$c_x + c_y + c_z \leqslant 1 \tag{20}$$

$$\nu \leqslant \{1 - (c_x + c_y + c_z)\}/\{2\cdot \mathrm{DT}(1/\mathrm{DX}^2 + 1/\mathrm{DY}^2 + 1/\mathrm{DZ}^2)\}. \tag{21}$$

As the combination of the centered and the donor-cell methods is employed in

the TUMMAC-IV method through the finite difference representation such as Eq. (7), the stability condition is modified as

$$(c_x + c_y + c_z)^2 \leqslant \alpha(c_x + c_y + c_z) + 2(d_x + d_y + d_z) \leqslant 1. \tag{22}$$

Equation (22) is rewritten as

$$(c_x + c_y + c_z) \leqslant \alpha \leqslant 1, \tag{23}$$

$$\nu \leqslant \{1 - \alpha(c_x + c_y + c_z)\}/\{2 \cdot \mathrm{DT}(1/\mathrm{DX}^2 + 1/\mathrm{DY}^2 + 1/\mathrm{DZ}^2)\}. \tag{24}$$

Equation (23) gives the condition to the combination factor α, while Eq. (24) gives only the lower limit of kinematic viscosity.

To secure stability of the SOR method in the solution procedure of the Poisson equation the following condition of the relaxation factor is required

$$0 \leqslant \omega < 2. \tag{25}$$

The above equations give only approximate necessary conditions, and the satisfaction of the above conditions does not always guarantee stable solutions. As much more complicated treatments that are beyond the governing equations are required especially on the body surface and the free surface, where unstable phenomena are liable to occur, careful effort must be devoted there to assure stability of the solution as described in the succeeding sections.

VI. Simplification of the Body Configuration and Flagging

The engineering purpose of the present TUMMAC-IV method is to compute the wave system and wave resistance generated by an advancing ship, taking account of the nonlinear features of the waves. Quantitative or qualitative accuracy of the estimation of wave resistance is very important for the hull-form optimization method, since the hull-form is very sensitive to wave resistance. For instance, the attachment of a properly designed bulbous bow can reduce wave resistance by 50 percent. This is why the configuration of a hull-form is particularly complicated at the forward and after ends, sometimes having bulbs or appendages. These unique aspects of the configuration of a hull form imply that careful treatment is required in the computation. In particular, the x-directional curve of a hull on an x–y horizontal plane (called the waterline) must be more carefully treated than the vertical curve of a hull on a y–z plane (called the frame-line).

The domain of computation is as illustrated in Fig. 5 for the case of a forebody of a ship. A half side of a ship body is included in the computational domain and a symmetry condition is imposed on the centerplane boundary. The uniform velocity U is parallel to the centerline and then the problem of a ship in straight course is treated.

The narrow restriction on the body configuration is a serious shortcoming of the

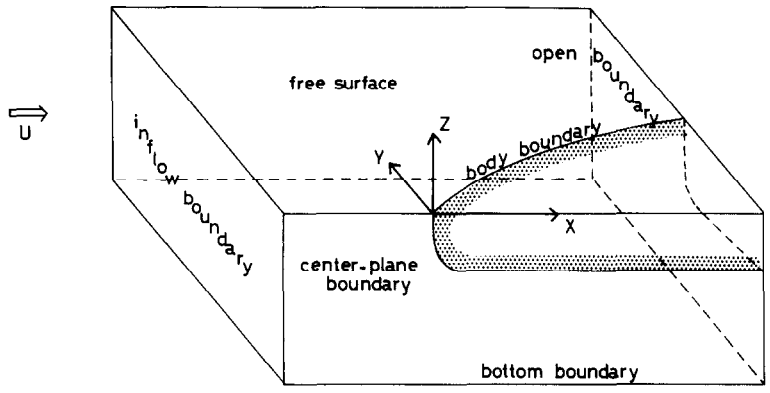

FIG. 5. Computational domain.

MAC method which results from the adoption of a rectangular cell system. The alternative is the adoption of a body-fitted coordinate system. But in the problems that contain free surface it is difficult and not economical to make coordinate transformation at every time step, taking account of the deformed free surface configuration as well as the 3D arbitrary ship hull configuration. Viecelli [6] developed the ABMAC (aribtrary boundary MAC) method in order to extend flexibility of the body configuration in 2D case. In the present TUMMAC-IV method a new treatment of a 3D arbitrary body boundary is made, partly taking account of the concept of the ABMAC method.

The hull configuration on the x–y plane, i.e., a waterline, is approximated by segments of straight line as seen in Fig. 6. The original waterline for the determination of the segments is that on the horizontal plane that includes the centers of cells. Then, the vertical variation of the hull configuration within a cell height is neglected and the body surface in a cell is assumed to be a vertical plane wall, of which the length is that of the segment and the height is DZ. Therefore, the vertical configuration (frame-line) is approximated by a step-like shape. A 3D sketch is shown in Fig. 7.

All the cells are flagged and classified into full-of-fluid cells (F-cells) body boundary cells (B-cells) and empty cells (E-cells) that do not contain fluid, i.e., a cell inside of the body boundary. A body boundary cell is a cell (1) that contains both fluid and body, (2) whose volume of fluid is more than a quarter of the volume of the cell and (3) which has at least one of six velocities not determined from the pressure gradient of Eq. (4). The cell whose volume of fluid is less than a quarter is defined as an empty cell, in which pressure is not computed. As the boundary cells must be continuously located along the succession of the segments, one of the outer neighboring cells of the above empty cell is newly defined as a body boundary cell, even when this cell does not contain body surface and violates the above condition (1). Some examples of cell division and the definition of B-cells are shown in

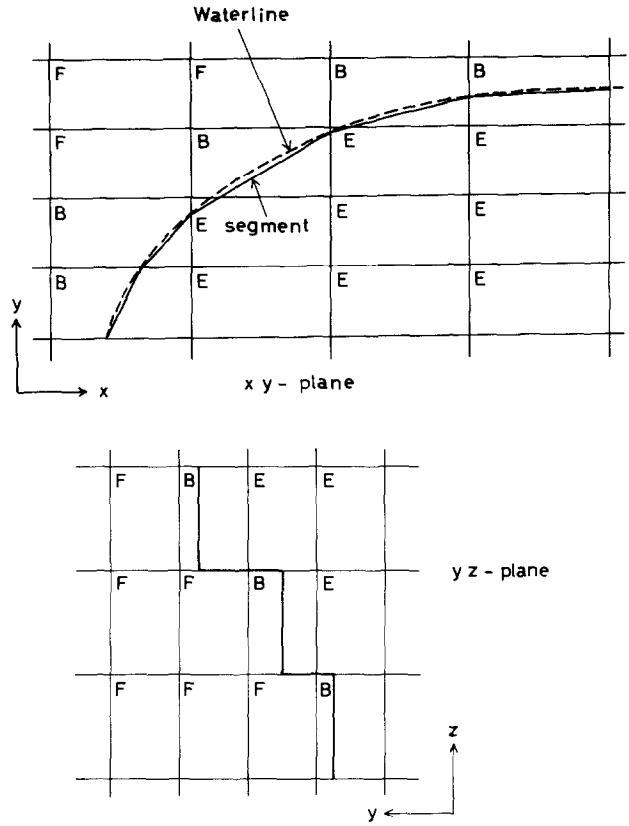

FIG. 6. Simplification of a hull form on horizontal (x–y) and vertical (y–z) planes.

Figs. 8–10 for the case of the hull form of a bulk carrier M55F0 which has a long parallel middle body. The cell denoted K is a special cell, to which the same procedure with an F-cell is applied with one zero-velocity of w on the body surface.

A body boundary cell is surrounded by four cells on a horizontal plane and two cells over and under it. The six surrounding cells are F-cells, B-cells, or E-cells. In both F- and B-cells the pressure is computed and the velocities facing these cells are computed through Eq. (4), but in an E-cell the pressure is not computed and the velocites facing an E-cell necessitate special treatment. Thus, the computational scheme of a body boundary condition varies depending on the sort of cells surrounding the concerned B-cell. Therefore all B-cells are classified into nine cases (ICASE = 0 to 8) depending on the flags of the four horizontally neighboring cells and into four cases (KCASE = 0 to 3) depending on the flags of the two vertically neighboring cells, as shown in Figs. 11 and 12. The case in which more than two of the horizontally neighboring cells are E-cells is not considered. If ICASE = 0 and KCASE = 0 simultaneously, the cell is not a B-cell.

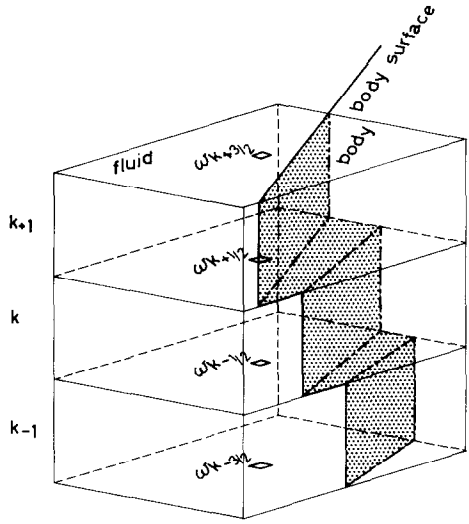

FIG. 7. Simplified body boundary configuration.

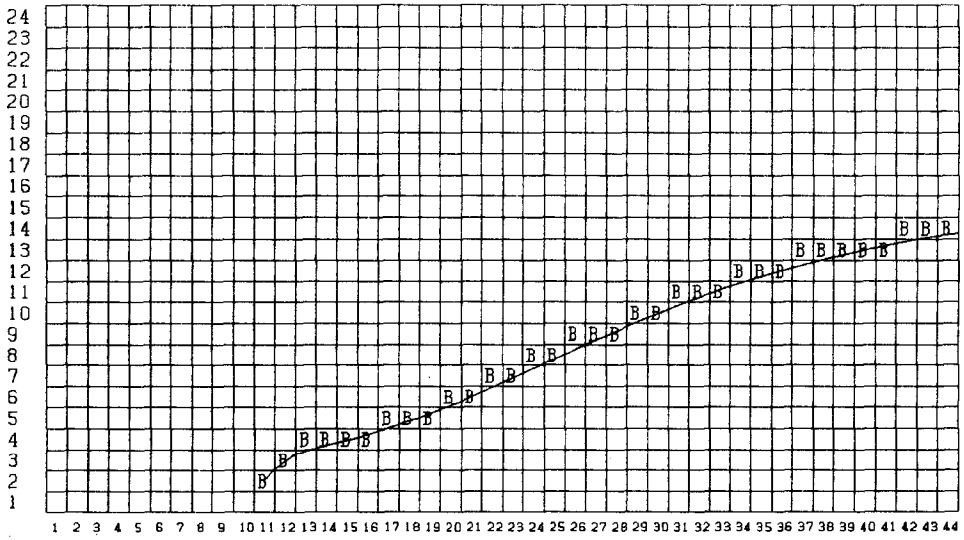

FIG. 8. Cell division on a horizontal (x–y) plane of M55F0 for a ballast condition.

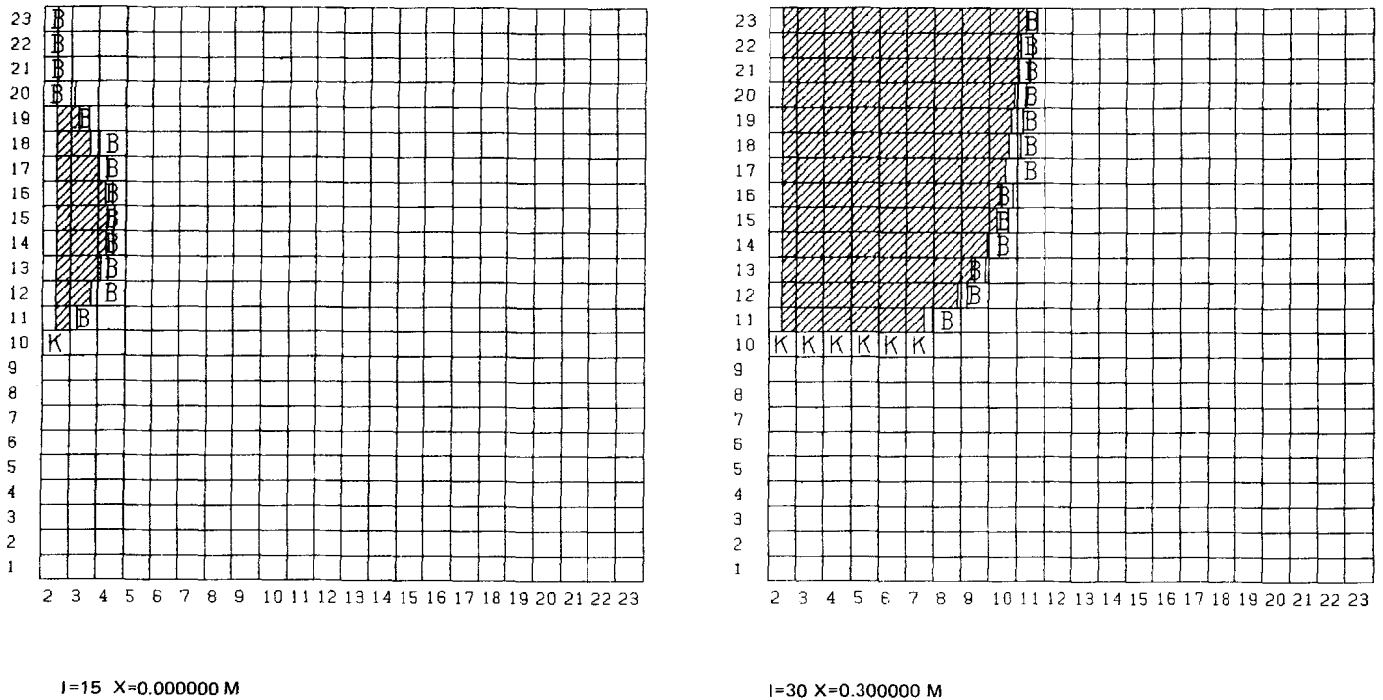

FIG. 9. Cell division on a vertical (y–z) planes of M55F0 for a ballast condition.

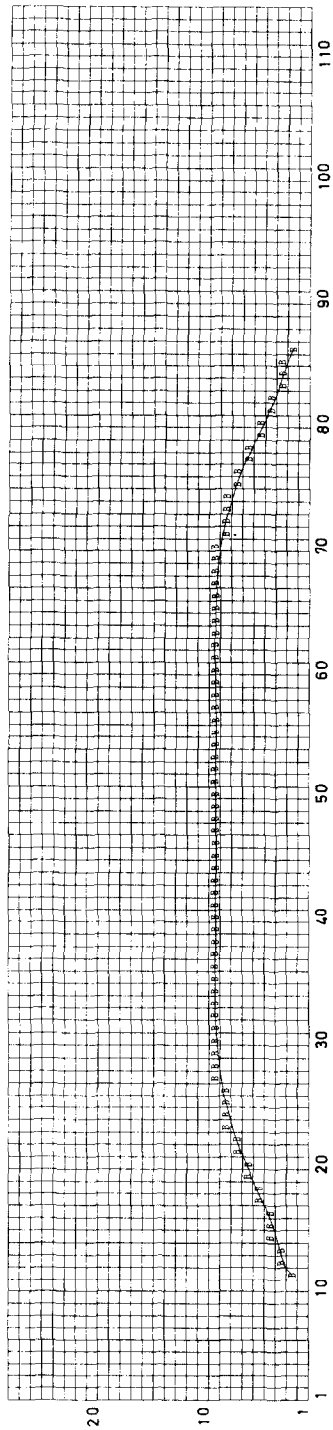

FIG. 10. Cell division on a horizontal x–y plane of the full length of M55F0.

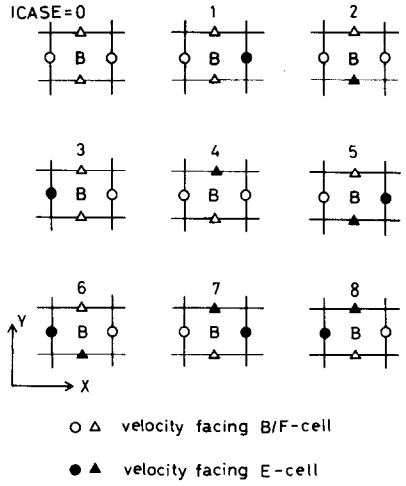

FIG. 11. Cases of a body boundary cell on a horizontal x–y plane.

VII. BODY BOUNDARY CONDITION

A free-slip body boundary condition is applied, because the cell size is not small enough to apply a no-slip body boundary condition. A free-slip condition is implemented in body boundary cells by satisfying the following three conditions: (1) the velocity normal to the body surface is zero; (2) the velocity tangential to the body surface does not have normal gradient; (3) the divergence of the cell is zero.

In a typical 2D case in which two inner velocities are not known, such as the case of ICASE = 5, the velocities U_2 and V_1 in Fig. 13 are set equal to U_1 and V_2 respectively to satisfy the condition (3) in the full volume of the B-cell and to approximately satisfy the condition (2). Then, the pressure of this B-cell Ψ_{ij} is varied by the following iterative equation (see [6])

$$\Psi_{i,j}^{m+1} = \Psi_{i,j}^{m} - \omega(\mathbf{V}_p \cdot \mathbf{n})/(2 \cdot \delta \cdot \mathrm{DT}). \tag{26}$$

Here, $\mathbf{V}_p$ and $\mathbf{n}$ are a fluid velocity vector at the center of the segment and a unit

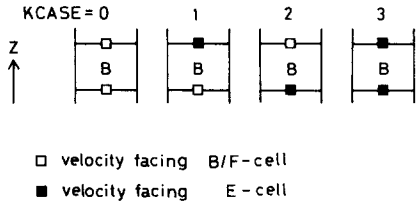

FIG. 12. Cases of a body boundary cell on a vertical plane.

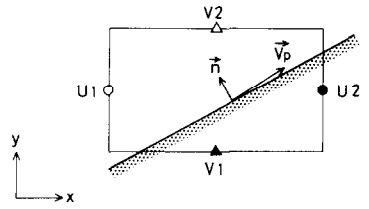

FIG. 13. Definition sketch for a body boundary cell.

outward normal vector of a segment, respectively. The two components of $\mathbf{V}_p$ are calculated from nearby velocities by linear interpolation. δ is a mesh parameter. Equation (26) means that the pressure in a boundary cell is adjusted so that the fluid flow across the segment is extinguished. When condition (1) is fulfilled, the zero-divergence condition for the fluid portion of the B-cell is satisfied, because the divergence of the full volume to the B-cell is already zero and fluid does not flow across the body boundary. Equation (26) is in a form similar to Eq. (16), and the successive computation of pressure in F-cells is smoothly continued to B-cells.

In the present 3D case the procedure is a little more complicated, but it basically follows the above procedure, which is, in a sense, a reasonable consequence of the simplification of the body configuration in the manner shown in Fig. 7. The body boundary is composed of vertical and horizontal panels, and one B-cell normally has one vertical boundary panel and two horizontal boundary panels. For the vertical panel the procedure above described in a 2D case is available, and for the two horizontal panels special consideration on the vertical velocity component w is made as described below.

First, the vertical velocity w of a B-cell is extrapolated from the velocities outside of the B-cell, when the vertically neighboring cell is not an E-cell,or it is set equal to zero, when an E-cell is next to it (see Fig. 12). Second, the divergence of the B-cell is given by the following equation:

$$D_{i,j,k} = (U_2 - U_1)/\mathrm{DX} + (V_2 - V_1)/\mathrm{DY} + (W_2 \cdot \mathrm{SF}_2 - W_1 \cdot \mathrm{SF}_1)/\mathrm{DZ}. \tag{27}$$

Here, U_1, U_2, V_1, and V_2 are as defined in Fig. 13, and W_1 and W_2 are vertical velocity component w on lower and upper surfaces of the B-cell, respectively. SF_1 and SF_2 are the dimensionless areas of "windows" on the lower and upper surfaces, respectively. The area of the "window" is that of a portion of the lower or upper surface that faces the fluid portion of the lower or upper B-cell, and it is made dimensionless by $\mathrm{DX} \cdot \mathrm{DY}$. Only through the "windows" is the fluid permitted to move vertically. Thus, some additional conditions are imposed on the velocity component w to approximately implement the 3D body boundary condition.

As W_1 and W_2 are determined beforehand in the manner described above, the zero-divergence condition of a B-cell is not fulfilled when U_2 and V_1 are set equal to

U_1 and V_2 as in the 2D case. Then the vertical divergence component $(W_2 \cdot \mathrm{SF}_2 - W_1 \cdot \mathrm{SF}_1)/\mathrm{DZ}$ is calculated and it is allotted to the velocities U_2, V_1 in Fig. 13 as

$$U_2 = U_1 + a$$
$$V_1 = V_2 + b \tag{28}$$

where

$$a/\mathrm{DX} - b/\mathrm{DY} + (W_2 \cdot \mathrm{SF}_2 - W_1 \cdot \mathrm{SF}_1)/\mathrm{DZ} = 0. \tag{29}$$

The values a and b are determined by two conditions, namely that the divergence of the cell is zero through Eq. (27), and that the velocity vector induced by (a, b) at the center of the segment is normal to the segment. Suppose that a and b in Eq. (28) are zero, then the inner velocities are set equal to the outer ones and no velocity gradient exists in the B-cell in Fig. 13. Therefore, the gradient of tangential velocity is scarcely produced, even if (a, b) does not induce tangential velocity at the center of the segment. Thus, the zero-divergence condition and the condition of zero-normal-gradient of tangential velocity are simultaneously satisfied.

After the inner velocities are determined in this way, the horizontal velocity vector $\mathbf{V}_p$ at the center of the segment is derived by linear interpolation. Then zero-normal-velocity condition is fulfilled by renewing $\Psi_{i,j,k}$ through the slightly modified form of Eq. (26), in which the subscript i,j is replaced by i,j,k and the mesh parameter δ is $(1/\mathrm{DX} + 1/\mathrm{DY} + 1/\mathrm{DZ})$.

The above procedure is repeated in the iterative process of the solution of the Poisson equation for the pressure. The new pressure $\Psi^{m+1}_{i,j,k}$ gives new velocities U_1 and V_2 in Fig. 13 and the new pressure field in the vicinity gives new velocities W_1 and W_2. The convergence of the repeated iterative cycle satisfies the 3D free-slip body boundary condition. Although some gross approximations are included in this procedure, it works well and the resultant pressure and velocity fields are legitimate.

B-cells do not always have two unknown velocities U_2 and V_1, but they have some other features as shown in Fig. 14. In the case of ICASE = 5, which is quite normal, the above-described procedure is applied; and in the other cases such as those of ICASE = 1 or 2 the procedure is slightly different. When ICASE = 1 or 2, only one inner velocity U_2 or V_1 respectively is not known. It is determined by the zero-divergence condition. In the case of ICASE = 1, for instance,

$$U_2 = U_1 - (V_2 - V_1)\,\mathrm{DX/DY} - (W_2 \cdot \mathrm{SF}_2 - W_1 \cdot \mathrm{SF}_1)\,\mathrm{DX/DZ}. \tag{30}$$

In this case, the treatment of body boundary cell is less rigorous than the case of ICASE = 5, since the condition of zero-normal-gradient of tangential velocity is not considered. However, this inadequacy is considerably compensated by the inner extrapolation of velocities as described below.

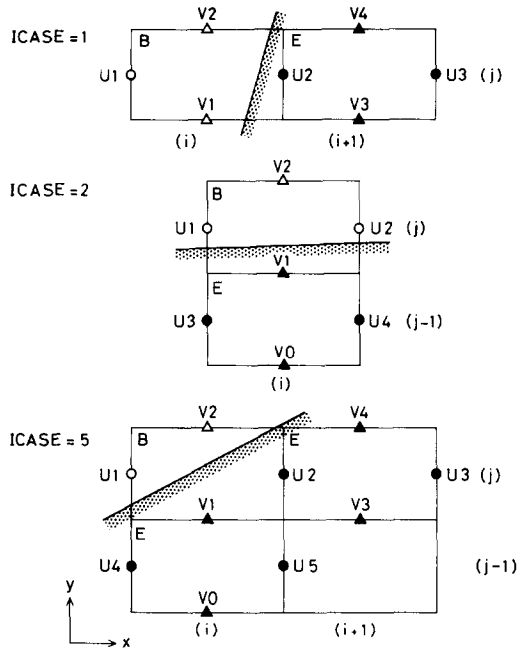

FIG. 14. Definition sketch for giving velocities inside of a body boundary.

Some other inner velocities, which are not yet determined in the above procedure to satisfy the body boundary condition, are necessary for the calculation of the convective term or the calculation of the vector of the movement of the marker particles. So the velocities such as U_3, U_4, U_5, V_0, V_3, V_4 in Fig. 14 are determined as follows: ICASE = 1,

$$\begin{aligned} U_3 &= U_2 \\ V_3 &= V_1 \\ V_4 &= V_2. \end{aligned} \tag{31}$$

ICASE = 2,

$$\begin{aligned} U_4 &= U_2 \\ V_0 &= V_1. \end{aligned} \tag{32}$$

This setting of velocity by Eqs. (31) and (32) is expected to work in a way to reduce

the normal gradient of the tangential velocity when the segment is nearly vertical or horizontal, respectively to ICASE = 1 and 2. In the case ICASE = 5,

$$\begin{aligned} U_3 &= U_2 \\ U_5 &= U_2 \\ V_3 &= V_1 \\ V_4 &= V_2. \end{aligned} \tag{33}$$

The velocity w of the inner E-cell is extrapolated from that of neighboring B-cells. It is noted that the above treatment of ICASE = 1 is common to the treatment of the foremost end cell where a stagnant flow is realized, even if the symmetry condition is applied as described in the following section.

VIII. Free Surface Condition

The free surface condition is another most important condition, because the nonlinearity of this condition is the source of the nonlinear wave-making, and the resistance due to the nonlinear waves plays a very important role in the resistance components.

Let the exact location of the free surface be $z = \zeta$, the exact inviscid free surface conditions on this location are

$$\Psi = \Psi_0 \tag{34}$$

$$\frac{D\zeta}{Dt} \equiv \frac{\partial \zeta}{\partial t} + u \cdot \frac{\partial \zeta}{\partial x} + v \cdot \frac{\partial \zeta}{\partial y} - w = 0. \tag{35}$$

Here, Ψ_0 is the atmospheric pressure P_0 divided by the density of water. Equation (34) is a dynamic condition and Eq. (35) is a kinematic condition and both are exact as long as the viscous stress and the surface tension are not considered. Both additional forces are safely assumed to be zero in high Froude-number flow problems.

For the fulfillment of the condition of Eq. (34) the "irregular star" of Chan and Street [5] is employed. In the solution procedure of the Poisson equation for the pressure near the free surface, such as the pressure $P_{i,j}$ in Fig. 15, the atmospheric pressure P_0 on the free surface is used instead of the pressure of the neighboring cells, taking account of the various lengths between pressure points, i.e., legs of the irregular star η_1, η_2, η_3, and η_4 in the 2D case of Fig. 15. Making use of Taylor's

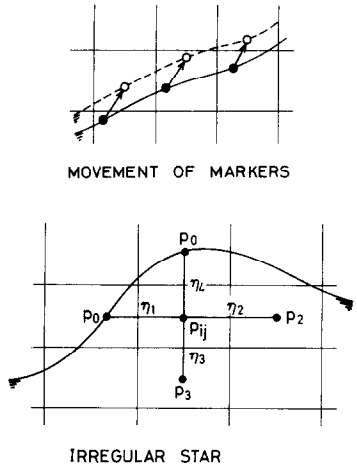

FIG. 15. Marker movement and "irregular star" in 2D case.

expansion of the neighboring pressure with respect to $P_{i,j}$ the approximate Poisson equation in a 2D case [5] becomes

$$\begin{aligned}\Psi_{i,k} = &\{\eta_1\eta_2\eta_3\eta_4/(\eta_1\eta_3+\eta_2\eta_4)\}\\ &\cdot[(\eta_3\Psi_1+\eta_1\Psi_3)/\{\eta_1\eta_3(\eta_1+\eta_3)\}\\ &+(\eta_4\Psi_2+\eta_2\Psi_4)/\{\eta_2\eta_4(\eta_2+\eta_4)\}-R_{i,k}/2].\end{aligned} \tag{36}$$

In the same way the 3D equation of the "irregular star" is

$$\begin{aligned}\Psi_{i,j,k} = &\{\eta_1\eta_2\eta_3\eta_4\eta_5\eta_6/(\eta_1\eta_2\eta_3\eta_4+\eta_3\eta_4\eta_5\eta_6+\eta_1\eta_2\eta_5\eta_6)\}\\ &\cdot[(\eta_2\Psi_1+\eta_1\Psi_2)/\{\eta_1\eta_2(\eta_1+\eta_2)\}\\ &+(\eta_4\Psi_3+\eta_3\Psi_4)/\{\eta_3\eta_4(\eta_3+\eta_4)\}\\ &+(\eta_6\Psi_5+\eta_5\Psi_6)/\{\eta_5\eta_6(\eta_5+\eta_6)\}-R_{i,j,k}/2].\end{aligned} \tag{37}$$

This computation of pressure in cells near the free surface through Eq. (37) is continued from the normal computation of the pressure in the cells below, in which the simultaneous iterative method is used.

The kinematic condition expressed by Eq. (35) is fulfilled by the use of marker particles located on the free surface. The marker particles move in a Lagrangian manner and their new location gives the new free-surface configuration. Let $(x_i, y_i,$

z_i) be the marker position and (u_i, v_i, w_i) be the flow velocities at this position, the new location at the $(n+1)$th time step is

$$\begin{aligned} x_i^{n+1} &= x_i^n + \mathrm{DT} \cdot u_i \\ y_i^{n+1} &= y_i^n + \mathrm{DT} \cdot v_i \\ z_i^{n+1} &= z_i^n + \mathrm{DT} \cdot w_i. \end{aligned} \tag{38}$$

The velocities (u_i, v_i, w_i) are each obtained from the velocities at the nearest nine velocity points by the nine-points interpolation method described below.

In the present 3D case only one marker particle is used for each free surface cell. When the initial location (x_i, y_i, z_i) is at the center of a cell, the new wave height is obtained at irregular positions on the disturbed water surface, which makes the interpolation of wave height difficult. Therefore, the initial positions of marker particles are iteratively calculated so that the new positions are located straight above the center of the cells as shown in a 2D case in Fig. 15.

The velocities above the free surface are necessary in the calculation of the convective terms and in the interpolation procedure to determine the starting positions and the velocities of movement of marker particles. They are linearly extrapolated from three velocities in the fluid. In the interpolation in this extended velocity field, the nine-points interpolation formula below is used:

$$\begin{aligned} U = U_0 &+ (a/2)(U_2 - U_1) + (c/2)(U_4 - U_3) \\ &+ (1/4)\{2a^2(U_2 + U_1 - 2 \cdot U_0) \\ &+ 2c^2(U_4 + U_3 - 2 \cdot U_0) \\ &+ ac(U_8 - U_7 - U_6 + U_5)\} \end{aligned} \tag{39}$$

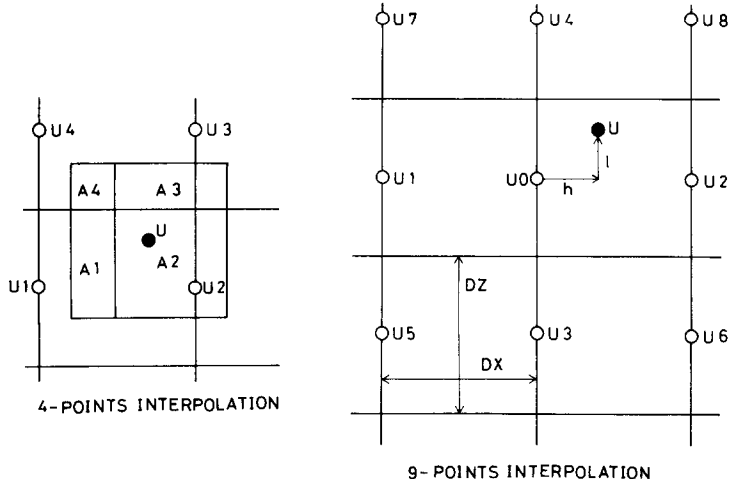

FIG. 16. Four- and nine-point interpolations.

where

$$a = h/\mathrm{DX}, \qquad c = 1/\mathrm{DZ}.$$

The definition sketch is shown in Fig. 16. The alternative interpolation formula is the four-points interpolation:

$$U = (A_1 \cdot U_1 + A_2 \cdot U_2 + A_3 \cdot U_3 + A_4 \cdot U_4)/(\mathrm{DX} \cdot \mathrm{DZ}). \tag{40}$$

The definition is shown in Fig. 16, in which A_1, etc. are areas of the divided portion of the cell. Equation (40) is a linear equation and Eq. (39) is a quadratic equation, and therefore higher accuracy is expected by the use of Eq. (39), although with presumable difficulty in stability. Equation (39) is used in the interpolation near the free surface.

In the boundary cell that contains free surface, the computation of pressure is basically the same way as with normal body boundaries. However, the pressure of the cell above this cell Ψ_{k+1} must be linearly extrapolated by use of Ψ_k in a B-cell and Ψ_0 on the free surface shown in Fig. 17 in order to determine velocity w on the upper surface of the concerned cell. Moreover, the relaxation factor for the iterative solution procedure is modified as below in order to promote convergence of the pressure, following Nichols and Hirt [16],

$$\omega' = 4\omega/\{4 - \omega(1 - \mathrm{DZ}/\Delta Z)\}. \tag{41}$$

Here, ΔZ is the distance from the pressure point to the free surface as shown in Fig. 17.

Some special treatments are employed to stabilize solution. One drops the second-order terms of Eq. (39), when used in body boundary cells; the other filters

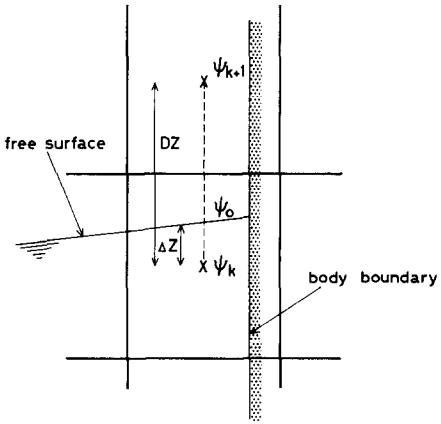

FIG. 17. Definition sketch for determining the relaxation factor for a boundary cell containing free surface.

wave height by the following formula which is used by Longuet-Higgins and Cokelet [17]:

$$\zeta_i' = (-\zeta_{i-2} - \zeta_{i+2} + 4\zeta_{i-1} + 4\zeta_{i+1} + 10\zeta_i)/16. \tag{42}$$

Equation (42) is used in the x direction and sometimes in the y direction as well.

IX. Centerplane Condition

The computational domain is bounded by a centerplane of a ship as seen in Fig. 5, because the fluid motion of a ship is symmetrical. The half body of a ship on the starboard side is considered, and then the pressure computation is advanced from centerplane to the side plane. On the centerplane the condition of symmetry must be taken into account, and its combination with the SOR procedure must be properly dealt with.

The centerplane bisects the cells in which pressure is first renewed as seen in Fig. 18. The boundary conditions are

$$\Psi_{i,1,k} = \Psi_{i,3,k} \tag{43a}$$

$$v_{i,3/2,k} = -v_{i,5/2,k} \tag{43b}$$

$$\eta_{i,3/2,k} = -\eta_{i,5/2,k}. \tag{43c}$$

For rigorous consideration of the centerplane boundary condition Eq. (43a) must be combined with the SOR procedure as below. Otherwise $\Psi_{i,1,k}$ is that of the mth iterative step, which violates the SOR procedure in a strict sense.

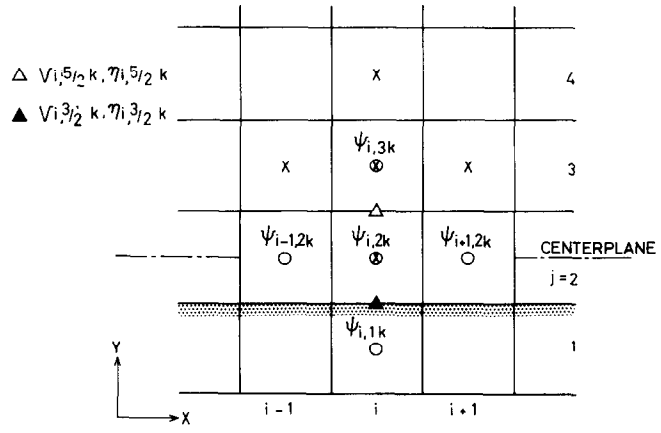

FIG. 18. Pressure points on centerplane boundary.

The iterative equations (14) for two pressures $\Psi^{m+1}_{i,2,k}$ and $\Psi^{m+1}_{i,3,k}$ in Fig. 18 are written as

$$\begin{aligned}\Psi^{m+1}_{i,2,k} &= (1-\omega)\Psi^{m}_{i,2,k} \\ &\quad + (\omega/\mathrm{AA})[(\Psi^{m}_{i+1,2,k} + \Psi^{m}_{m-1,2,k})/\mathrm{DX}^2 \\ &\quad + (\Psi^{m}_{i,3,k} + \Psi^{m+1}_{i,1,k})/\mathrm{DY}^2 \\ &\quad + (\Psi^{m}_{i,2,k+1} + \Psi^{m+1}_{i,2,k-1})/\mathrm{DZ}^2 - R_{i,2,k}], \end{aligned} \tag{44}$$

$$\begin{aligned}\Psi^{m+1}_{i,3,k} &= (1-\omega)\Psi^{m}_{i,3,k} \\ &\quad + (\omega/\mathrm{AA})[(\Psi^{m}_{i+1,3,k} + \Psi^{m+1}_{i-1,3,k})/\mathrm{DX}^2 \\ &\quad + (\Psi^{m}_{i,4,k} + \Psi^{m+1}_{i,2,k})/\mathrm{DY}^2 \\ &\quad + (\Psi^{m}_{i,3,k+1} + \Psi^{m+1}_{i,3,k-1})/\mathrm{DZ}^2 - R_{i,3,k}]. \end{aligned} \tag{45}$$

$\Psi^{m+1}_{i,1,k}$ in Eq. (44) is replaced by $\Psi^{m+1}_{i,3,k}$ from the boundary condition, and then Eq. (44) and (45) are simultaneous equations for two unknowns $\Psi^{m+1}_{i,2,k}$ and $\Psi^{m+1}_{i,3,k}$, which are easily solved. In $R_{i,2,k}$ of Eq. (44) $\eta_{i,3/2,k}$ is included and it is replaced by the known value from Eq. (43c).

However, a numerical test fortunately shows that the use of $\Psi^{m}_{i,1,k}$ instead of $\Psi^{m+1}_{i,1,k}$ does not give rise to an unfavorable effect at all. Then the simpler method is used in the TUMMAC-IV procedure.

X. Outer Boundary Condition

At the inflow boundary u values of the double model computed beforehand are imposed. This is safely acceptable when the disturbances due to the ship are scarcely noticed at the inflow boundary.

In the iterative solution procedure of the Poisson equation by the SOR method, the pressure $\Psi_{0,j,k}$ in Fig. 19 must be properly given for the computation of $\Psi_{1,j,k}$. The rigorous procedure of the SOR method necessitates the use of $\Psi_{0,j,k}$ of the $(m+1)$th iterative step, and it leads to a complicated procedure at the inflow boundary in a way similar to the centerplane condition [11]. However, a numerical test shows that this rigorous treatment does not contribute to any improvement as far as the ship wave problems are concerned. On the contrary, the simplest method, in which $\Psi_{0,j,k}$ is fixed to the value of the previous time step, provides successful

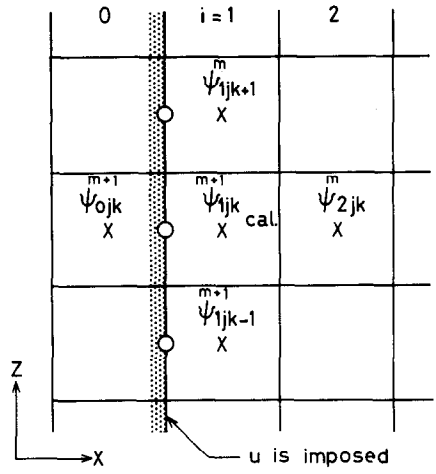

FIG. 19. Velocity and pressure points at inflow boundary.

results without serious problems. Therefore, this simplest method is employed in the TUMMAC-IV procedure.

The bottom boundary is usually located so deep that the fluid motion is very gentle. Then, hydrostatic pressure is given and velocities are constantly extrapolated below the boundary (see Fig. 20).

There are two open boundaries on which a radiation condition must be satisfied. This boundary condition is most difficult to fulfill. In the TUMMAC-IV method the conditions of TUMMAC-I [9] are followed. At the sideward open boundary u, v, w, and P are set equal to the inner values so that their gradient in the direction normal to the boundary is set at zero. At the rear open boundary their gradient along the local flow direction is also set at zero. These simple conditions do not give unfavorable influences, partly because the combination of the centered and the donor-cell methods is employed for the convective terms of momentum equations. The transportive property of the donor-cell method, which means that disturbances do not propagate upstream, is presumably helpful for the fulfillment of the open boundary condition.

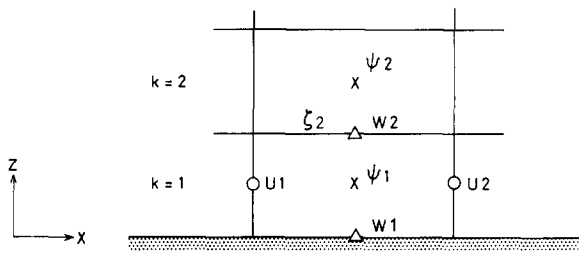

FIG. 20. Velocity and pressure points on bottom boundary.

XI. Computed Results of Ships with Vertical Side-Walls

In this section some computed results of ship models whose side-walls are vertical are presented. The simpler version TUMMAC-II is used here. The step-like approximation of the vertical configuration (frame-line) can be avoided for this hull form and the treatment of the body boundary condition is more reasonable without approximate consideration of the vertical velocity component. The combination factor α of the convective terms is assumed to equal 1.0, i.e, the donor-cell differencing is employed so that stable solutions can be obtained without difficulties.

Two simplified bulk carrier hulls M53A and M53C on ballast load condition and two parabolic waterlined hulls WM-1B and WM-1C, with and without a gigantic bulb of vertical cylinder type, are chosen for the computation. The principal particulars of these ship models are listed in Table I. The length of the full-scale ship of M53A or C is 150 m and the deadweight tonnage is about 23,000 tons, while the computation is made for the ship models of 3 m length. This bulk carrier hull-form is that of a middle speed ship which sails at a speed somewhat faster than large oil tankers. M53A and C have the same volume (displacement), and only the longitudinal distribution of the volume is different between them. The longitudinal configuration (waterline) of WM-1C is a parabolic curve and WM-1B is produced by attaching to it a gigantic bulb whose radius of the circle at the fore-end is 40 mm. The hull-forms of WM-1B and 1C are far from practical ships and they are chosen in order to know the difference of wave-making due to the difference of the fore-end configuration, i.e., blunt end and sharp end.

The conditions of computation are tabulated in Table II. Only the fore part of the ship model is included in the computational domain. The length of the fore part

TABLE I

Principal Particulars of Ship Models

Name of hull	M53A M53C	WM-1B WM-1C	Wigley's hull	M55F0
Type of hull	Simplified bulk-carrier	Parabolic waterline with and without blunt bow	Horizontally and vertically parabolic configuration	Practical bulk-carrier
Length (L) (m)	3,000	2.400	2.500	3.000
Breadth (B) (m)	0.509	0.240	0.250	0.497
Draft (d) (m)	0.100	0.100	0.156	0.090
Computed Froude number	0.180	0.240	0.267 0.289 0.316	0.180

TABLE II

Condition of Computation

Name of hull		M53A M53C	WM-1B WM-1C	Wigley's hull	M55F0
Domain of computation	length (m)	1.650	1.400	5.750	4.500
	breadth (m)	0.600	0.400	0.600	0.900
	depth (m)	0.400	0.340	0.313	0.270
Cell size	DX (mm)	50	25	25	40
	DY (mm)	20	16	15	36
	DZ (mm)	25	20	31.3	18
Approximate number of used cell		17000	27000	76000	42000
Time increment	DT (s)	0.00252	0.00252	0.00420 0.00388 0.00355	0.00461
Tme steps for acceleration		360	360	400	300
Total time steps		480	600	1200	600
Combination factor α		1.0	1.0	0.5	0.5
Relaxation factor ω		1.5	1.5	1.5	1.5
Kinematic viscosity ν (m^2/s)		0	0	0	1.139×10^{-6}
Froude number F_n		0.180	0.240	0.267 0.289 0.316	0.180
Speed of advance (m/s)		0.991	1.164	1.323 1.429 1.565	0.976

computed is 1.2 m for M53A and C and 1.0 m for WM-1B and 1C. The uniform flow is gradually accelerated for 360 time steps with very low acceleration at the beginning and at the end of acceleration stage. The Froude number Fn is defined as $U/\sqrt{g \cdot L}$, where U is the speed of advance and L is the ship length. The Froude number 0.18 is chosen for M53A and C, because it corresponds to their service speed, and 0.24 is chosen for WM-1B and 1C.

Computed time evolution of wave contour maps of M53A and C are shown in Figs. 21 and 22. Because the apex angle of M53A is larger than M53C the waves around the fore-end of M53A are higher. But, on the contrary, M53C generates waves of greater magnitude at the hollow surface at $x/d = 3$ to 4. As a total, the waves generated by M53A are less conspicuous, and as a result the wave resistance that M53A receives is smaller than M53C. Since the superiority of M53A cannot be

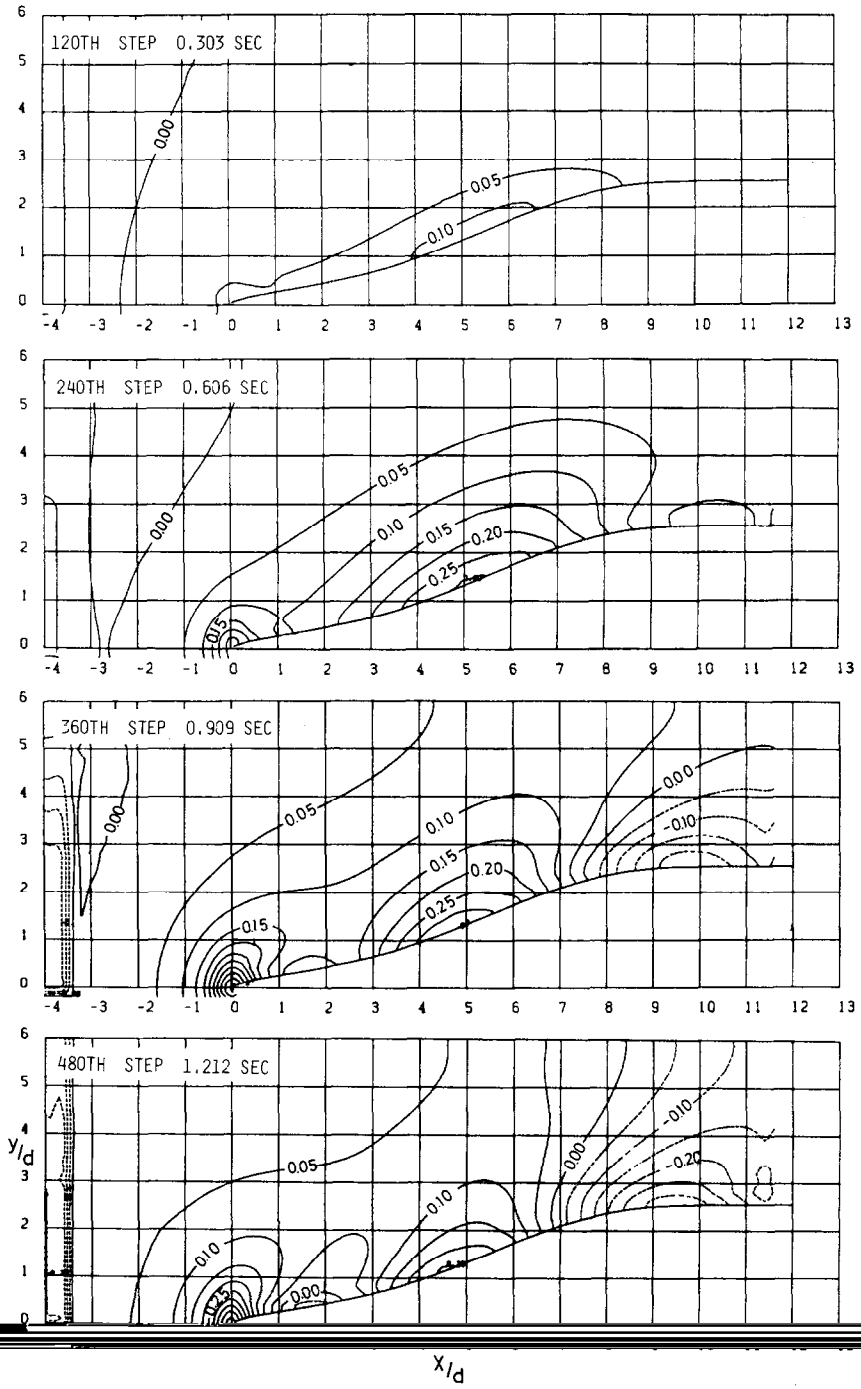

FIG. 21. Time evolution of wave height contours of M53A, steady advance speed of Fn = 0.18 (0.991 m/s) is reached at the 360 th time step. Positive values are contoured by solid isopleths and negative values by dashed contours. The interval of contours is 0.05 H ($= U^2/2g$).

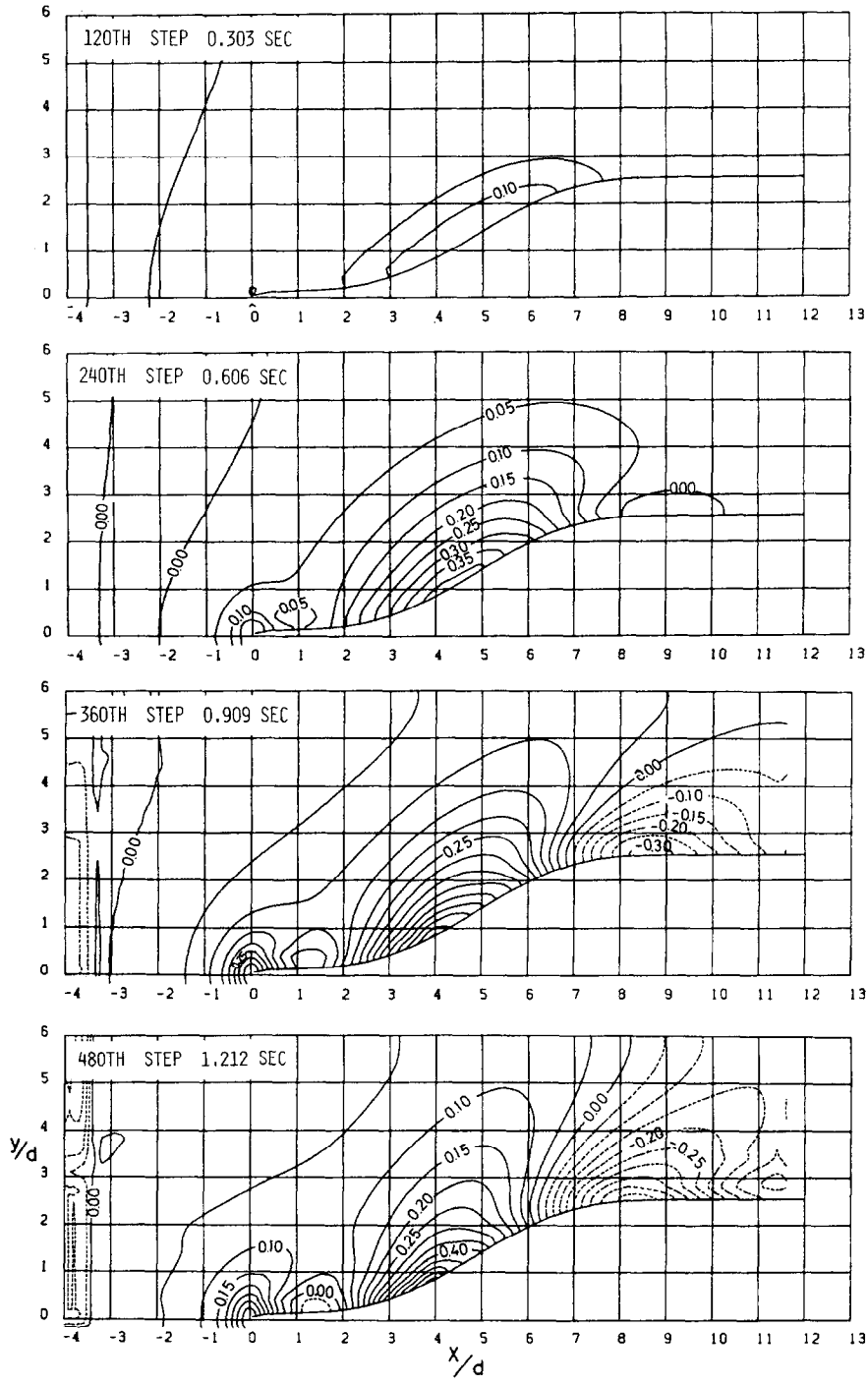

FIG. 22. Same as Fig. 21, for the M53C.

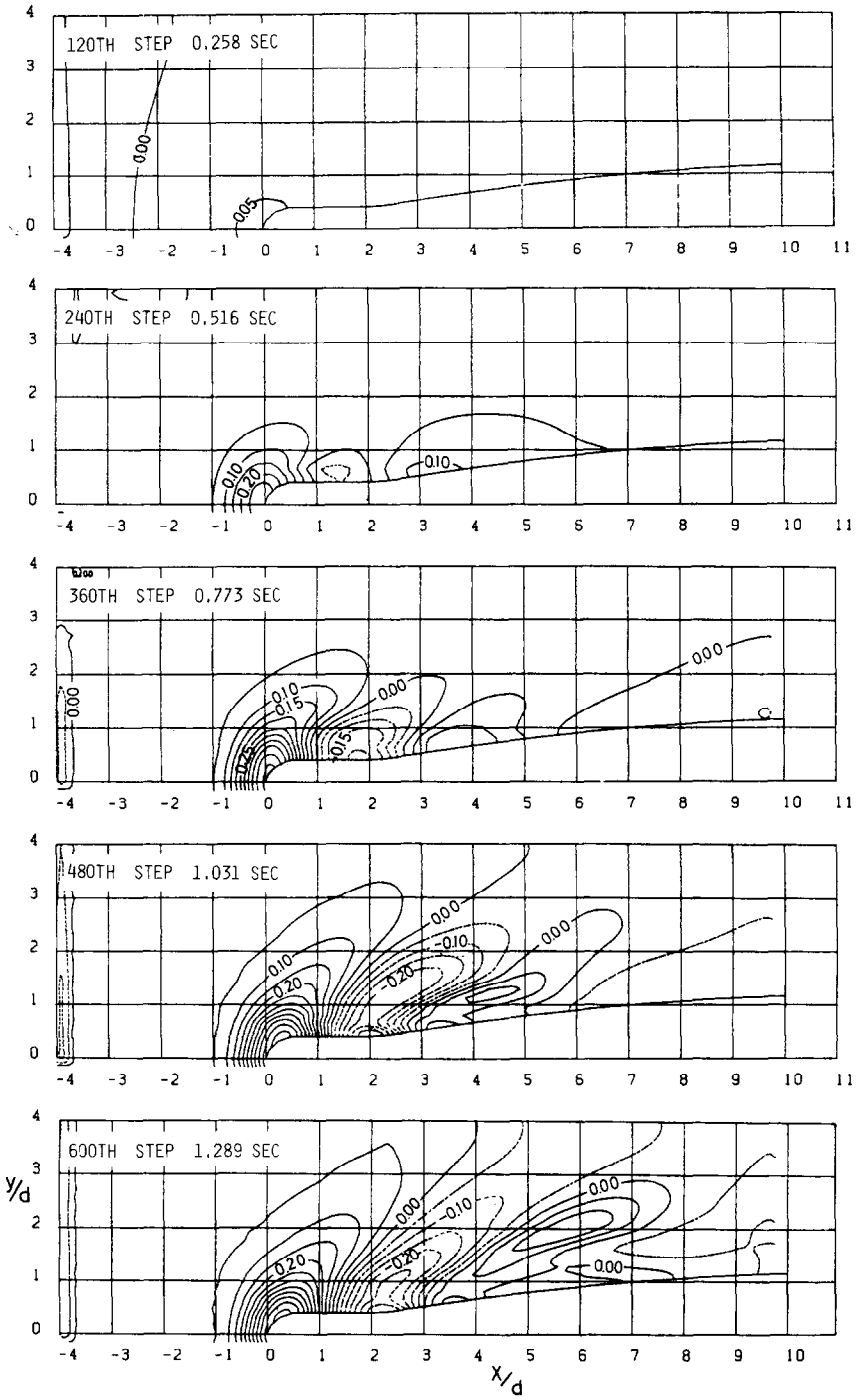

FIG. 23. Time evolution of wave height contours of WM-1B, steady advance speed of Fn = 0.24 (1.164 m/s) is reached at the 360th time step. The interval of contours is 0.05 H.

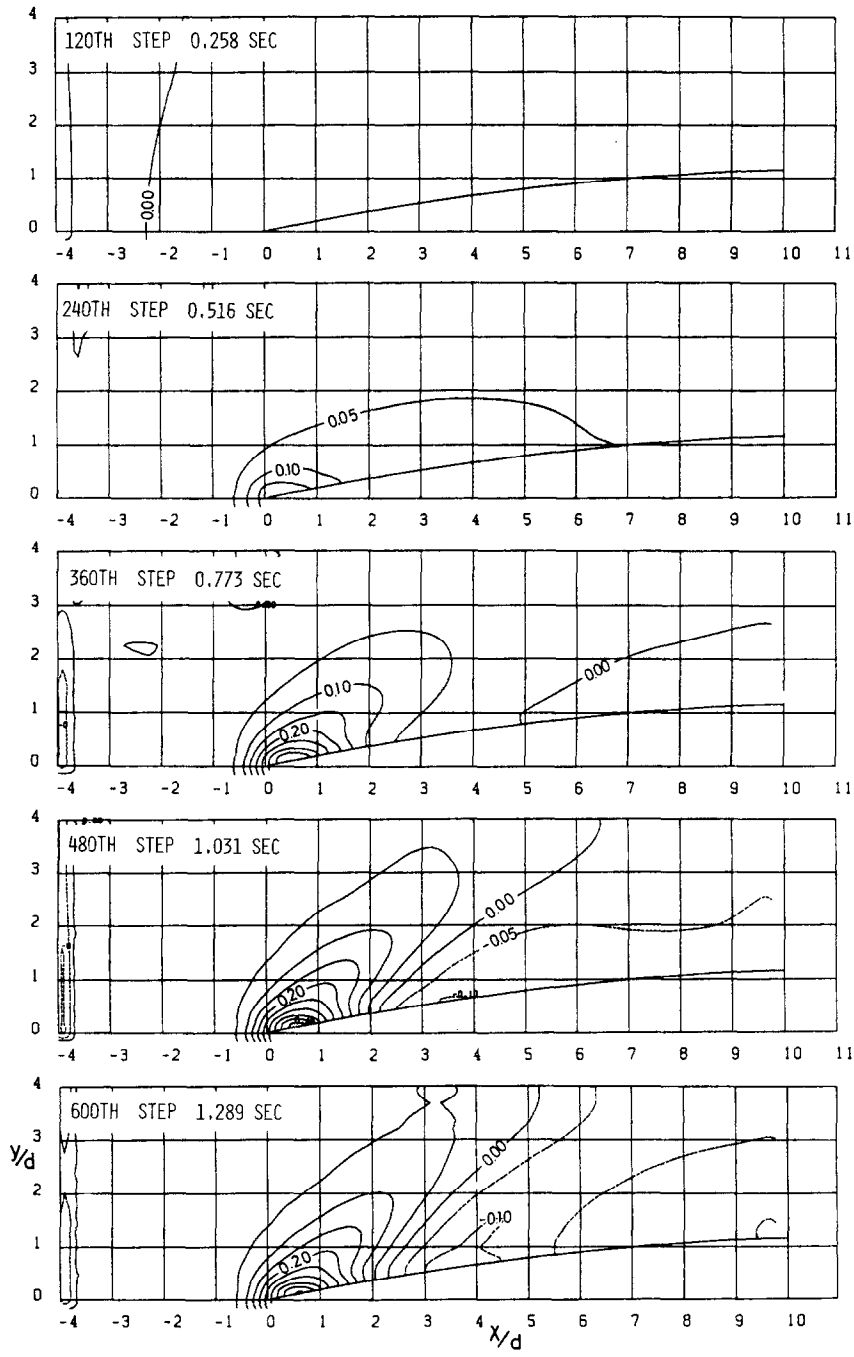

FIG. 24. Same as Fig. 23, for the WM-1C.

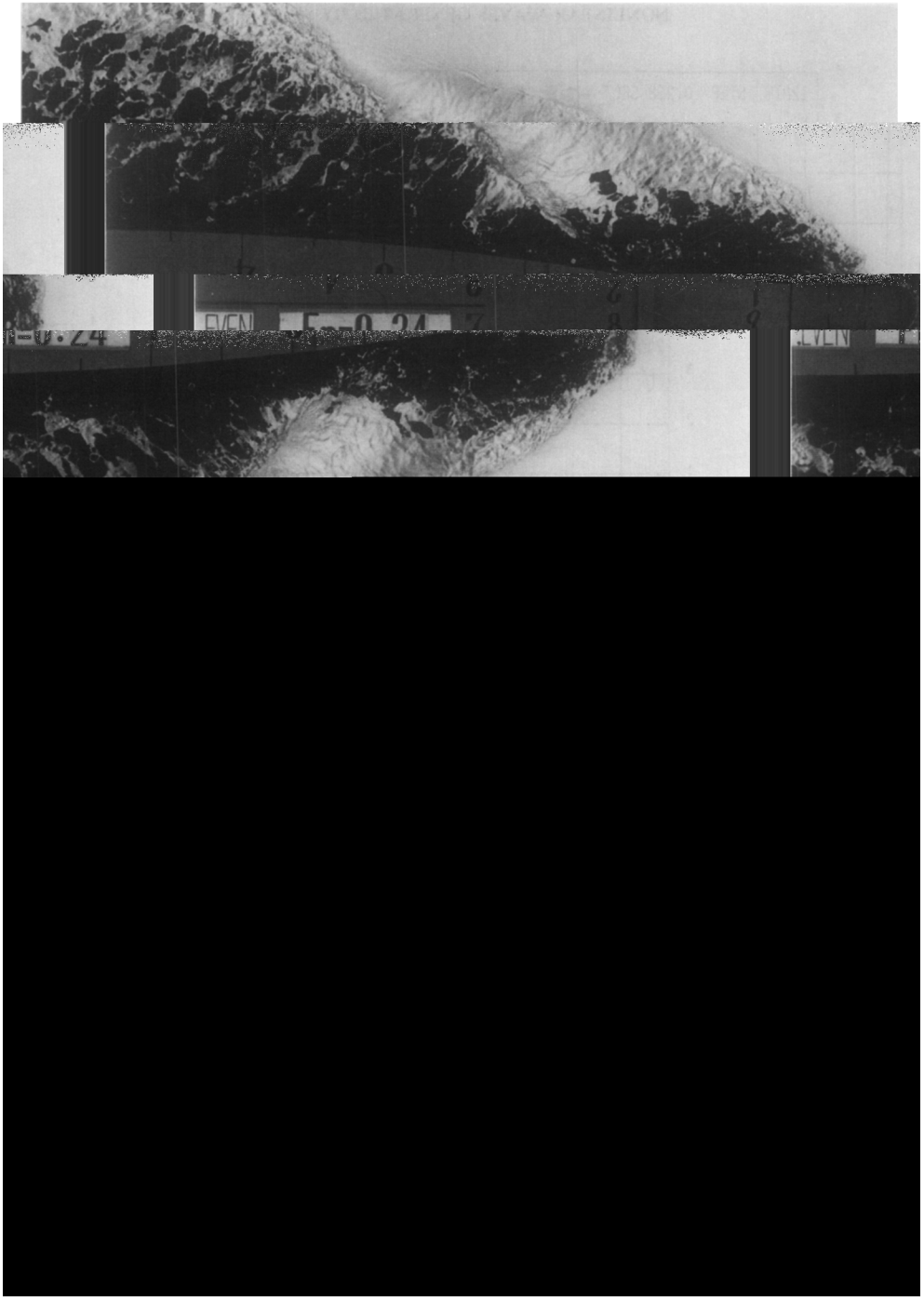

FIG. 25. Photographs of waves of forebodies of WM-1B (above) and WM-1C (below) advancing at Fn = 0.24 (1.164 m/s).

explained by linear wave-making theories or by experimental measurement of the linear wave system that spreads far away, the numerical simulation of waves in the near-field is very useful for the correct qualitative estimation of wave resistance.

The computed time-evolutional contour maps of waves generated by WM-1B and 1C are shown in Figs. 23 and 24. The gigantic bulb of vertical cylinder type produces a very intense foremost wave which has a circular plan form, accompanied by a very deep trough and crest. In the case of WM-1C, which has a pure parabolic waterline, only the foremost wave is conspicuous. The modesty of the waves of WM-1C in comparison to WM-1B is evident. The photographs of the waves of these two simple models are shown in Fig. 25. The waves of WM-1B are so intense and steep as to cause violent wave breaking at the wave front. Although the numerical results do not explain all of the complicated features of nonlinear waves around a bow, they succeed in simulating the intensity and steepness of the waves of the hull with a gigantic bulb.

XII. Computed Results of Ships of Complete Three-Dimensional Configuration

Two ship models with complete 3D configuration are chosen here, i.e., a ship model with simple mathematical curves called Wigley's model and a bulk carrier model M55F0 with a typical practical hull form. Principal particulars are shown in Table I. The combination of the donor-cell and centered differencing is used for the convection terms with the combination factor 0.5. The kinematic viscosity is neglected in the computation with Wigley's hull and that of actual fresh water is used in the computation with M55F0. This difference gives only negligible difference in fluid flow, because a free-slip body boundary condition is employed and the diffusion term influences waves only very slightly.

The hull surface of the Wigley's model is made of parabolic curves as defined by

$$y = (B/2)\{1-(2x/L)^2\}\{1-(z/d)^2\}. \tag{46}$$

Here, L, B, and d are ship model length, breadth, and draft (depth below the undisturbed free surface), respectively. The hull form of M55F0 has a bulbous bow and a semi-transom stern with a small stern bulb. It is one of the typically well-designed hull forms for a single-propellered bulk carrier of 26,000 deadweight tonnage. The load conditon is ballast condition (lightly loaded condition) with small draft. On this condition the difference of hull form is sensitively revealed by wave-making.

Computations were conducted mostly for the full length of the two ship models, and the conditions of the computations are tabulated in Table II. Three steady advance speeds of Fn = 0.267, 0.289, and 0.316 are chosen for the Wigley's hull and Fn = 0.180 is chosen for M55F0 which corresponds to the service speed of 13.5 knots.

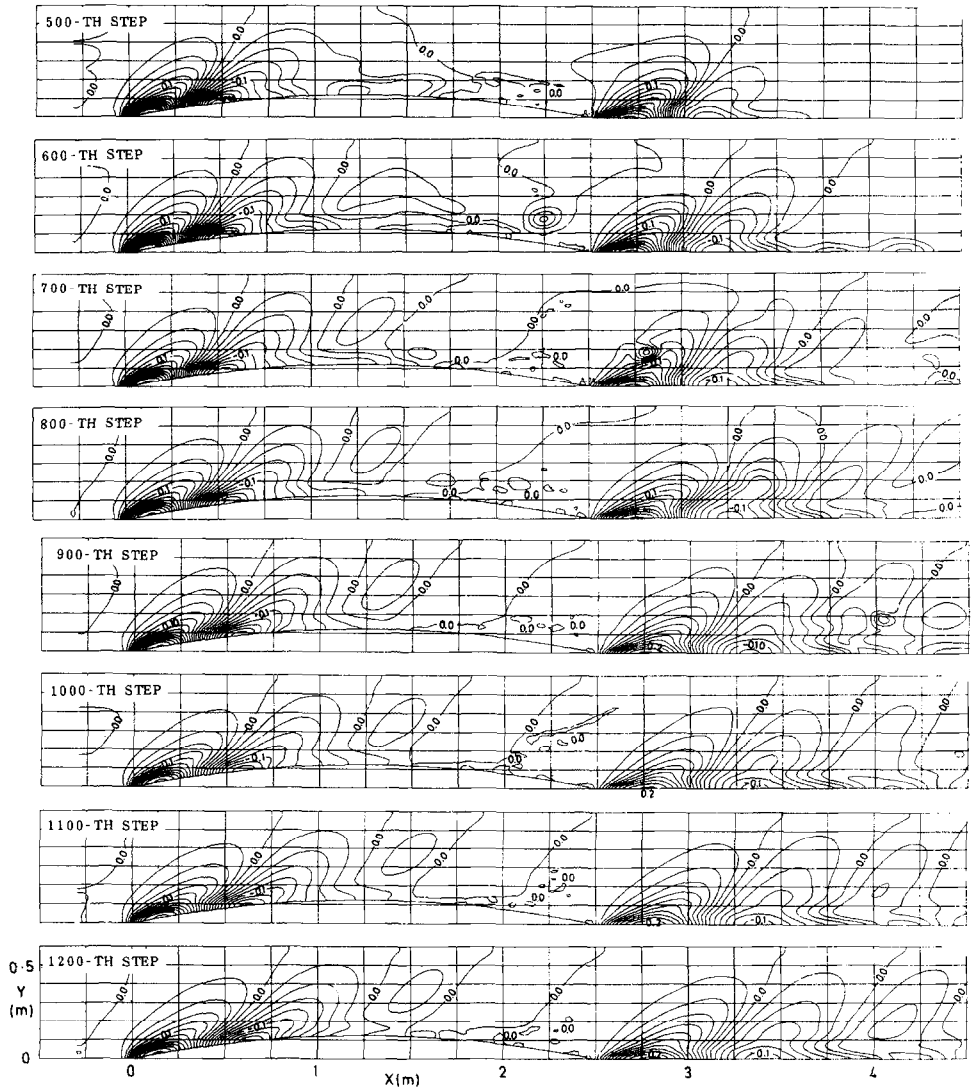

FIG. 26. Time evolution of wave height contours of the Wigley's hull from 500th to 1200th time step at the interval of 100 time steps. Steady states of Fn = 0.267, 0.289, and 0.316, are reached at the 600th, 900th and 1200th time steps. Both positive and negative values are contoured in solid curves. The contour interval is 0.02 H ($= U^2/2g$).

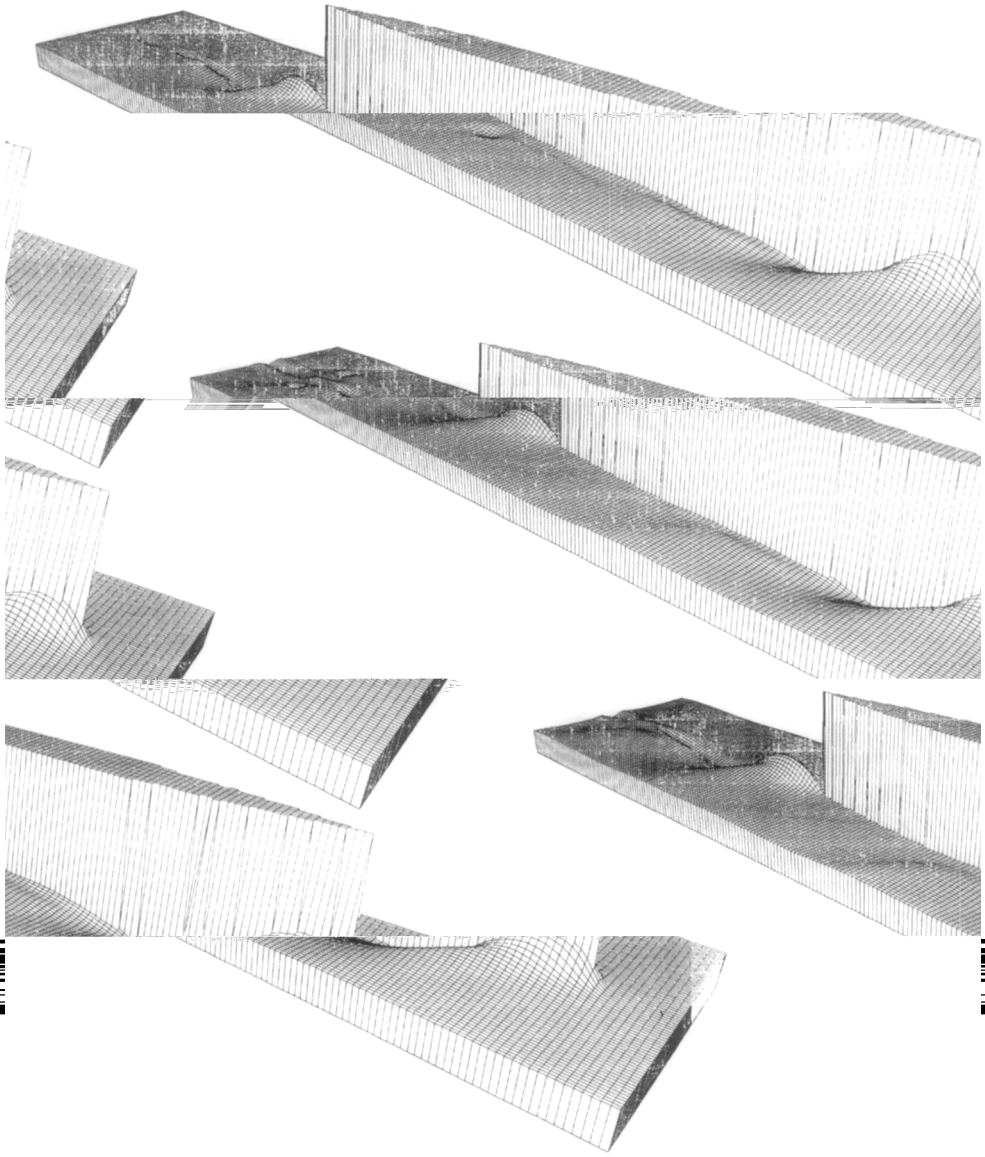

FIG. 27. Perspective views of waves of the Wigley's hull at Fn = 0.267, 0.289, and 0.316 from above.

The computation of the fluid motion around the Wigley's hull at three speeds of advance was carried out continuously for 1200 time steps. The computation is started from the condition of rest and the uniform stream is accelerated for 400 time steps until it reaches to 1.323 m/s which corresponds to Fn = 0.267. The uniform stream is kept constant for 200 time steps and a steady solution of Fn = 0.267 is obtained at the 600th time step. Then, the uniform stream is accelerated again for

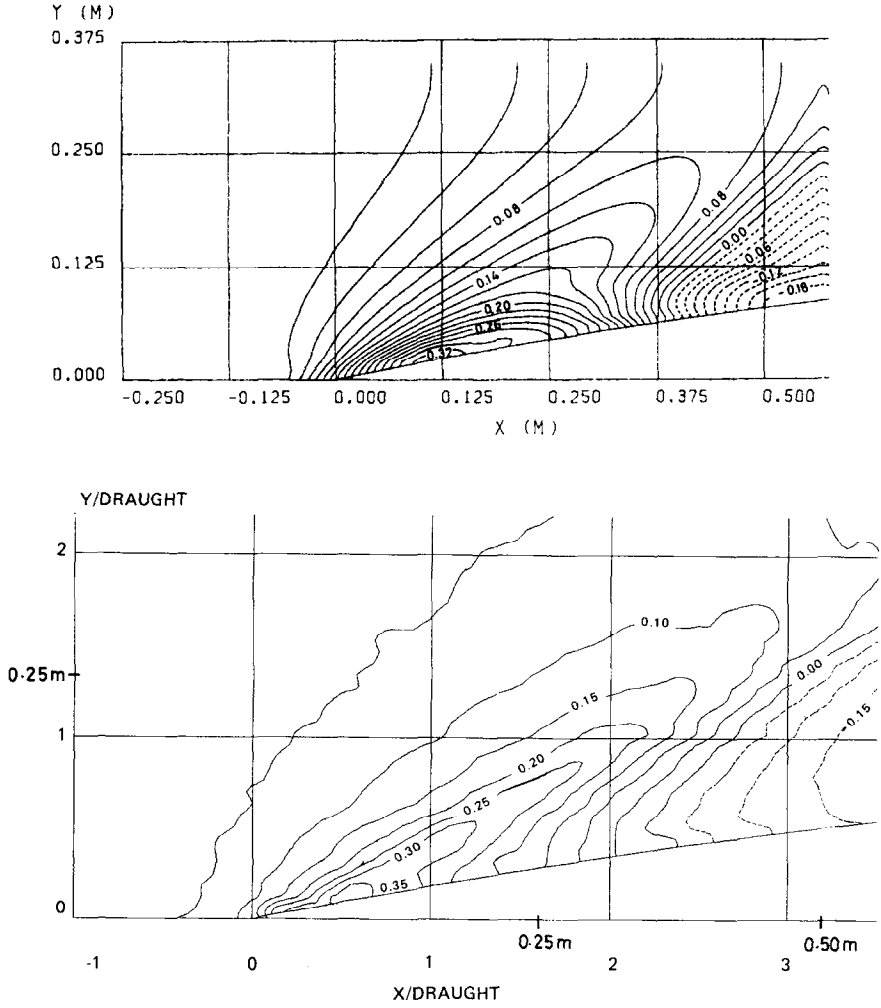

FIG. 28. Comparison of computed (above) and measured (below) wave height contour maps of the Wigley's hull at Fn = 0.289.

100 time steps and the steady state of Fn = 0.289 is reached at the 900th time step. It is once more accelerated and the solution at Fn = 0.316 is finally obtained at the 1200th time step. The dimensionless time increment $DT \cdot U/d$ is kept constant throughout. The number of iterations per time step is from 18 to 30 with a mean of about 24. This typical number of iterations is approximately the same for other computational cases in this paper. As the number of cells in which pressure is computed is approximately 76,000, the CPU time required by the super-computer HITAC S-810/20 was nearly 3 hr.

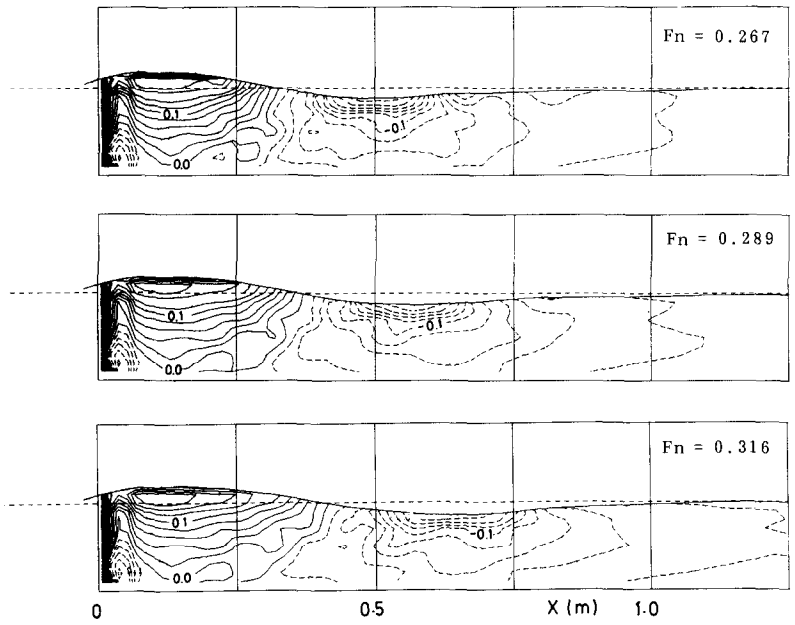

FIG. 29. Pressure distribution on the hull surface of the forebody of the Wigley's hull at Fn = 0.267, 0.289, and 0.316 from above. Positive values are contoured by solid isopleths and negative values by dashed contours. The interval ΔCp is 0.02.

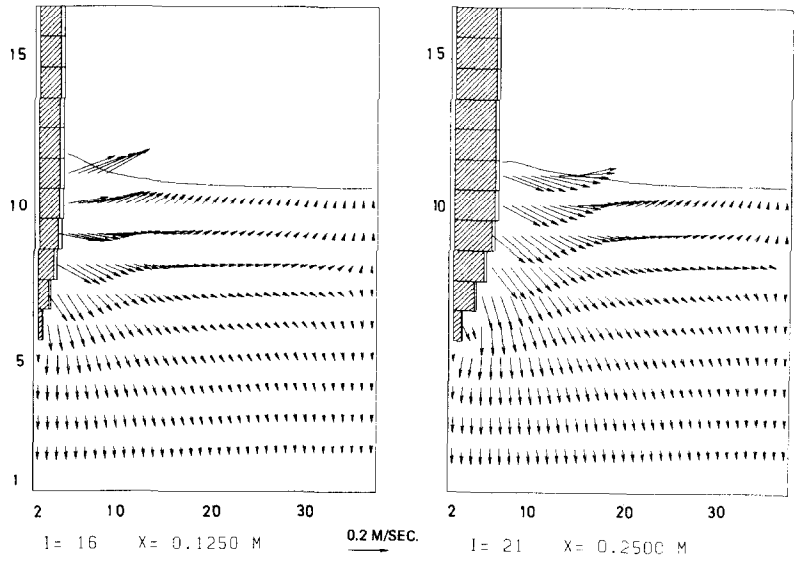

FIG. 30. Velocity vector fields on vertical y–z planes of the Wigley's hull advancing at Fn = 0.316.

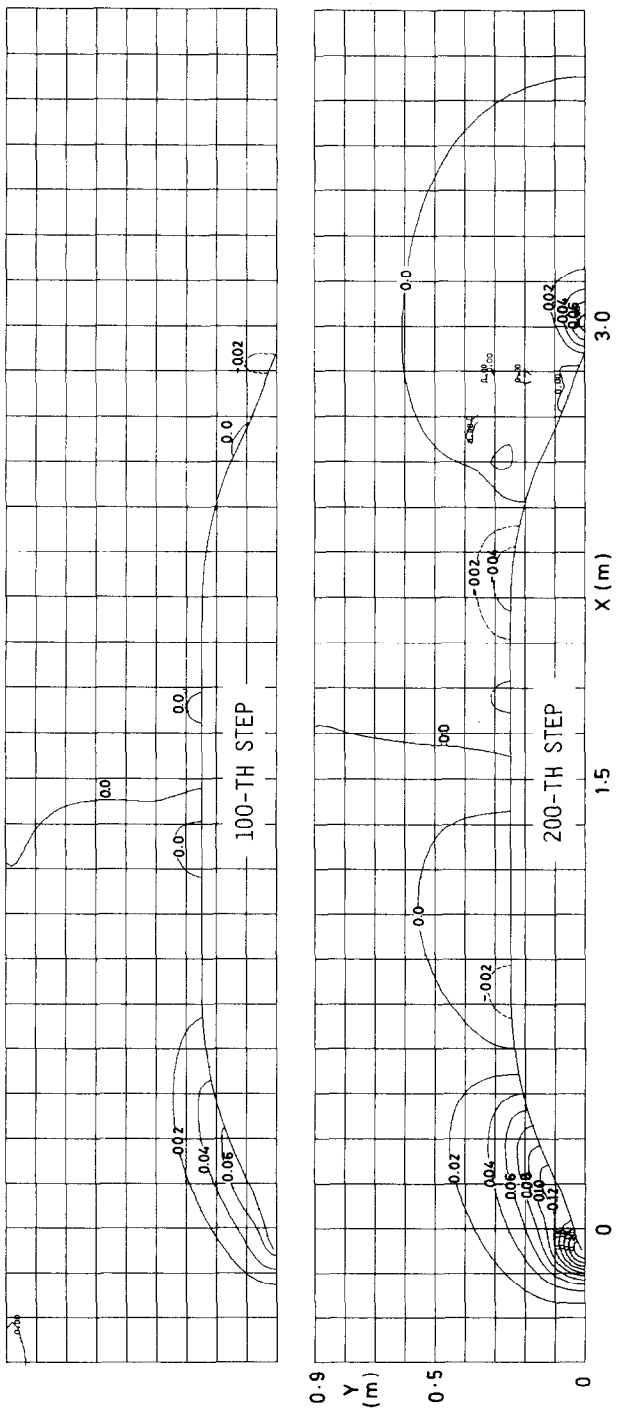
100-TH STEP
200-TH STEP
0.0
0.002
0.04
0.06
0.02
0.08
0.1
0.12
-0.002
-0.04
0
1.5
3.0
X (m)
0.9
0.5
0
Y (m)

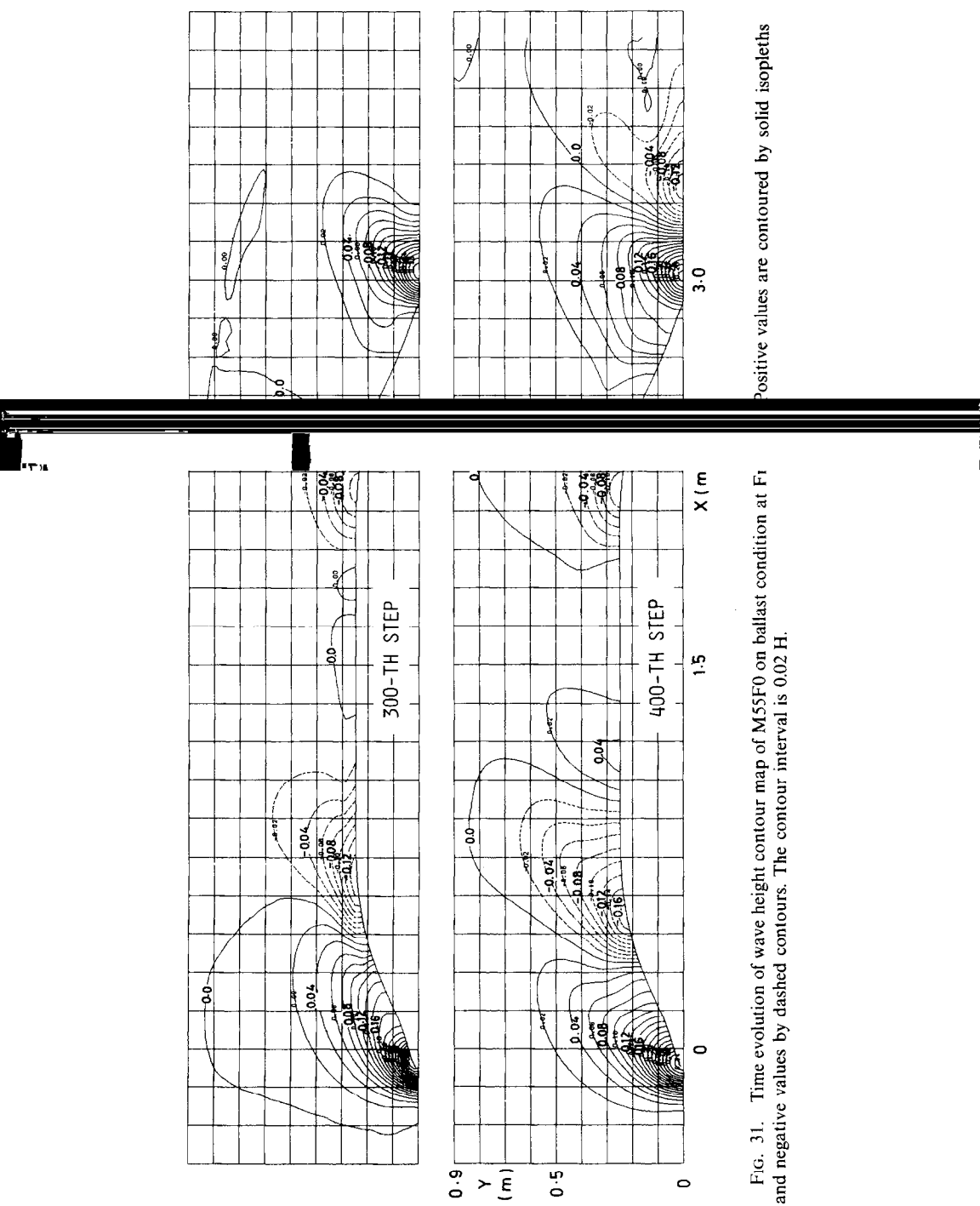

FIG. 31. Time evolution of wave height contour map of M55F0 on ballast condition at Fr and negative values by dashed contours. The contour interval is 0.02 H. Positive values are contoured by solid isopleths

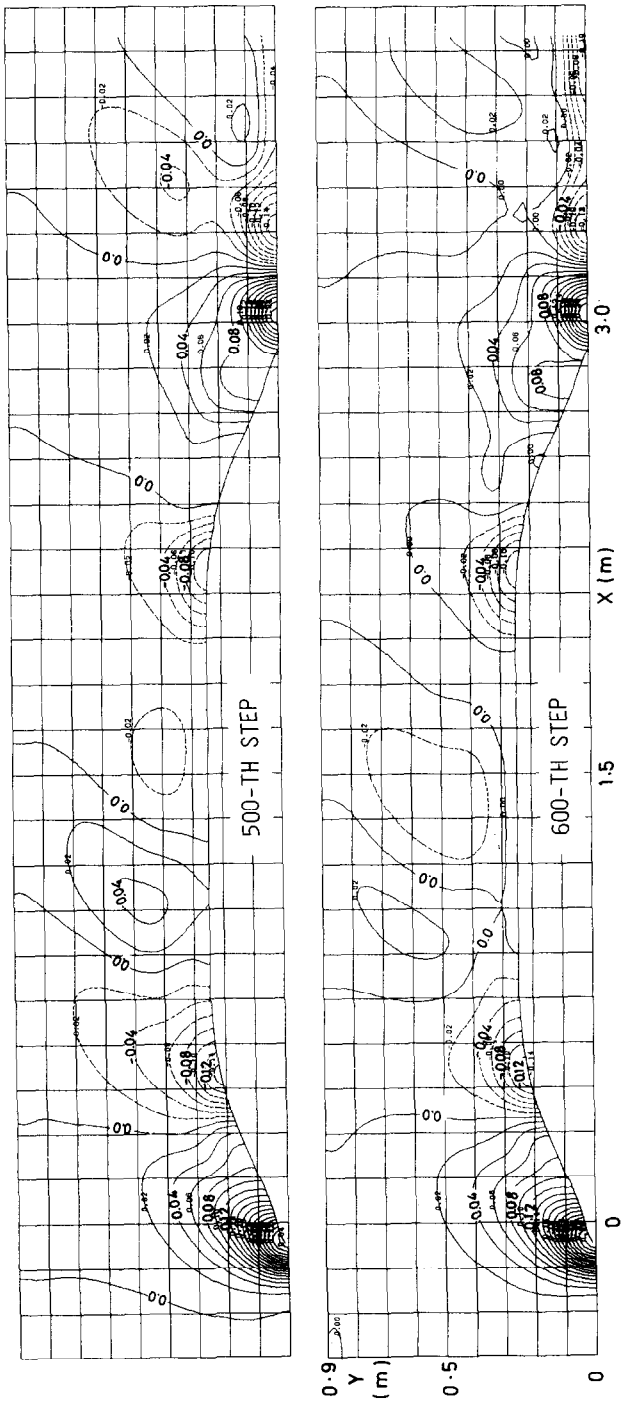

FIG. 31—Continued.

The computed time evolution of the wave height contour map is shown in Fig. 26 and the perspective views of waves at three steady speeds of advance are shown in Fig. 27. The contour is drawn at the interval of 0.02 H, where H is the head of uniform stream $U^2/2g$, and the contours are dimensionless. As the hull form is very fine, conspicuous waves occur from near the bow and the stern. The angle of wave crest of the foremost wave to the centerline decreases with the increase of advance speed, and simultaneously the maximum value of the contour decreases to 0.30 H, 0.28 H, and 0.24 H at Fn = 0.267, 0.289, and 0.316, respectively. This tendency is one of the typical characteristics of nonlinear bow waves.

Computation of waves in the local area was also carried out and the results are compared with experimental values in Fig. 28. The cell dimensions DX, DY, DZ are 25, 10, and 31.3 mm, respectively, which is a little better than the case of Fig. 26. The agreement is satisfactory, but the discrepancy is clear on the back side of the foremost wave where turbulence of free surface is likely to be produced.

The computed contour maps of pressure coefficient of the forebody of a Wigley's hull are shown in Fig. 29, and some examples of velocity field are shown in Fig. 30. By the finite difference computation with 76,000 cells, 304,000 values of velocity components and pressure are simultaneously derived, which is absolutely impossible in experimental research. Among these data the pressure distribution on the body surface and the velocity field in the near-field are of particular importance, because the integration of the former is directly equal to the resistance and the velocities of the latter give details of the wave motion. Figure 29 indicates that the high pressure region is generated at the fore-end and near the wave crest. Resistance reduction will be attained by reducing the high pressure region near the bow by attaching a bulbous bow or some modification of the hull form.

The computed time evolution of the wave contour map of M55F0 is shown in Fig. 31. The horizontal cell division is as shown in Fig. 10, and it is very coarse considering that the protrusion of the bulbous bow is about 80 mm, while DX is 40 mm. In spite of this, the body boundary and the free surface conditions work

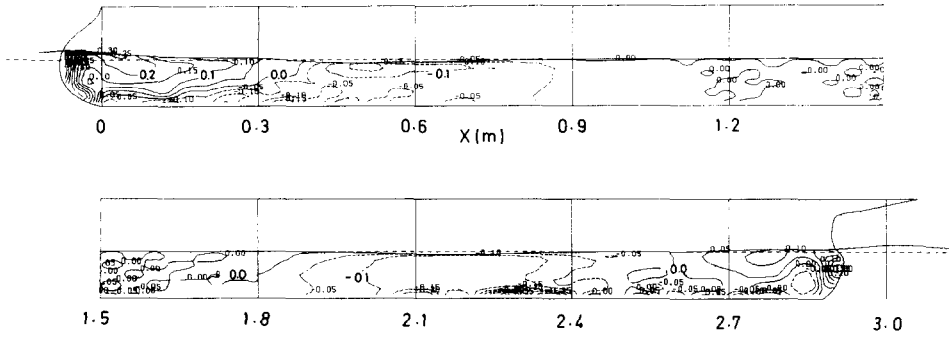

FIG. 32. Pressure distribution on the body surface of M55F0 for the ballast condition at Fn = 0.18, 600th time step. The contour interval ΔCp is 0.05.

very satisfactorily on this very complicated hull form, and the generation of the waves is well simulated.

The computed pressure distribution is shown in Fig. 32 in the form of contour map. The high pressure regions are located at the foreward and after ends, and at the free surface near both ends. The resistance is obtained by integrating the longitudinal component of pressure, but it is very difficult to obtain accurate values. The ship hull is pushed backward at the bow and pushed forward at the stern, and the resistance is the difference of the two forces. Besides, the afterbody is affected by viscous fluid motion which is very difficult to resolve theoretically taking into account its interaction with wave motion.

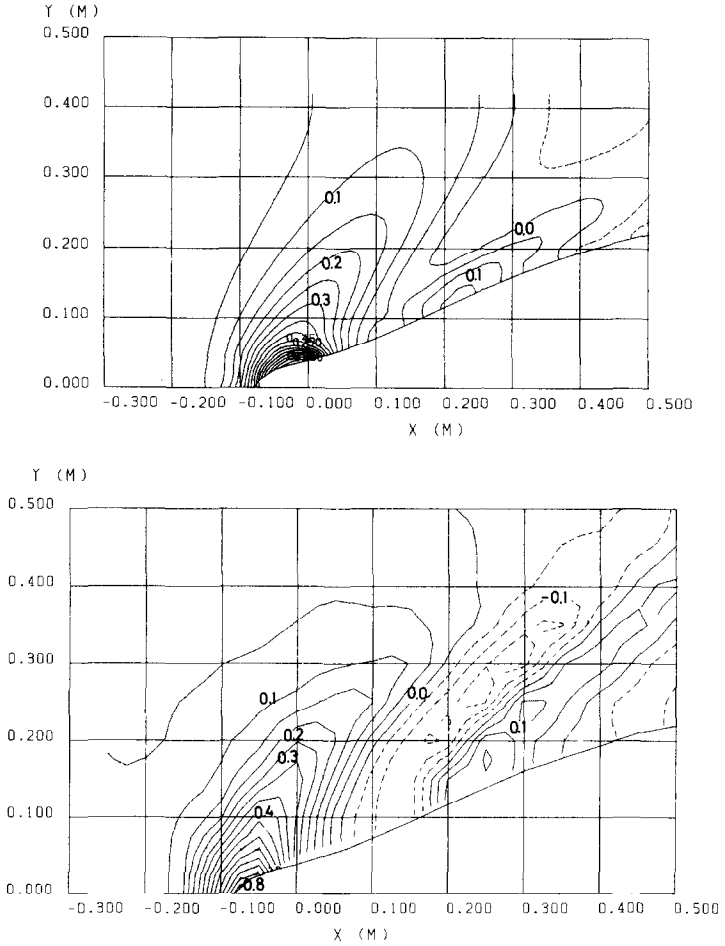

FIG. 33. Comparison of computed (above) and measured (below) wave height contour map of the forebody of M55F0 for the ballast condition at Fn = 0.18. The contour interval is 0.05H.

A finer cell division is employed for a part of the forebody of M55F0. The cell dimensions DX, DY, and DZ are 20, 20, and 18 mm, respectively. The computed wave height contour map is compared with an experimental one in Fig. 33. The discrepancy is in the fact the trough behind the foremost wave is vague in the computation. However, it is supposed that the present method can be succesfully applied to the design of actual hull forms.

XIII. Concluding Remarks

A finite difference simulation method for ship waves was developed by synthesizing many previous works of finite difference techniques of researchers in various scientific fields and by improving the techniques to suit the concerned 3D problem with free surface. Special efforts were devoted to the implementation of all the boundary conditions. In particular, the body surface and free surface conditions were difficult to fulfill with any degree of stability.

Although the computed results do not show complete agreement with experimental ones, the degree of agreement is guaranteed to be improved by using finer cells. Today the hull form of a ship is designed mostly by relying on the experimental results, partly because linear wave-making theories are not reliable enough. Experiments of deriving wave resistance are laborious and costly. A towing basin of more than 100 m length and very precise ship models must be prepared. When the qualitative accuracy of the TUMMAC-IV method is guaranteed, in other words, when the superiority of one hull form among many can be correctly explained, the numerical method can partly take the place of the towing basin. Moreover, the computational cost, which is expensive for the computations in this paper, will be rapidly decreased with the development of the computer. In the future the so-called numerical towing basin will play a significant role in the procedure of designing hull forms.

All the computations were carried out by HITAC M-200H/280H and HITAC S-810/20 (supercomputer) of the Computer Center, the University of Tokyo.

Acknowledgments

The authors are indebted to Mr. A. Suzuki of Ishikawajima-Harima Heavy Industries, Mr. K. Aoki of Kawasaki Heavy Industries, and Dr. T. Hino of the Ship Research Institute who worked hard for the development of the other versions of the TUMMAC method and gave the authors valuable suggestions when they were post-graduate students at the authors' laboratory. The authors gratefully acknowledge the supervisory work by Professor H. Kajitani and the careful typewriting of the manuscript by Miss S. Nigo. This research is supported partly by the Grant-in-Aid for Scientific Research of the Ministry of

REFERENCES

1. H. MIYATA, "Proceedings 13th Symposium on Naval Hydrodynamics", p. 335, (1980).
2. H. MIYATA, T. INUI, AND H. KAJITANI, *J. Soc. Naval Arch. Japan* **147** (1980), 1.
3. H. MIYATA AND T. INUI, *Adv. Appl. Mech.* **24** (1984), 215.
4. J. E. WELCH, F. H. HARLOW, J. P. SHANNON, AND B. J. DALY, "The MAC Method", Los Alamos Scientific Lab. Report LA-3425, Los Alamos, N. M., 1966.
5. R. K.-C. CHAN AND R. L. STREET, *J. Comput. Phys.* **6** (1970), 68.
6. J. A. VIECELLI, *J. Comput. Phys.* **8** (1971), 119.
7. B. D. NICHOLS AND C. W. HIRT, *J. Comput. Phys.* **12** (1973), 234.
8. H. MIYATA, A. SUZUKI, AND H. KAJITANI, "Proceedings 3rd International Conference on Numerical Ship Hydrodynamics," 37, 1981.
9. A. SUZUKI, H. MIYATA, H. KAJITANI, AND M. KANAI, *J. Soc. Naval Arch. Japan* **150** (1981), 143.
10. A. MASUKO, H. MIYATA, AND H. KAJITANI, *J. Soc. Naval Arch. Japan* **152** (1982), 33.
11. K. AOKI, H. MIYATA, A. MASUKO, AND H. KAJITANI, *J. Soc. Naval Arch. Japan* **154** (1983), 17.
12. H. MIYATA, K. AOKI, AND H. KAJITANI, *J. Soc. Naval Arch. Japan* **155** (1984), 1.
13. C. W. HIRT, B. D. NICHOLS, AND N. C. ROMERO, "SOLA—A Numerical Solution Algorithm for Transient Fluid Flows," Los Alamos Scientific Lab. Report LA-5852, Los Alamos, N. M., 1975.
14. P. J. ROACHE, "Computational Fluid Dynamics," Hermosa, Albuquerque, N. M., 1976.
15. C. W. HIRT, *J. Comput. Phys.* **2** (1968), 339.
16. B. D. NICHOLS AND C. W. HIRT, *J. Comput. Phys.* **8** (1971), 434.
17. M. S. LONGUET-HIGGINS AND E. D. COKELET, *Proc. R. Soc. London A* **350** (1976), 1.